



UNIVERSITAT POLITÈCNICA DE CATALUNYA  
BARCELONATECH

Departament de Teoria del Senyal  
i Comunicacions

# High-Resolution Space-Borne and Ground-Based SAR Persistent Scatterer Interferometry for Landslide Monitoring

Author

**Rubén Iglesias González**

Thesis Advisors

Jordi J. Mallorquí Franquet  
Xavier Fàbregas Cànovas

A Thesis submitted to the Universitat Politècnica de Catalunya  
(UPC) in partial fulfillment of the requirements for the degree of  
DOCTOR OF PHILOSOPHY

Ph.D. program on Signal Theory and Communications  
Remote Sensing Laboratory (RSLAB) Group  
Barcelona, September 2015

# 3

## CHAPTER 3

# THE COHERENT PIXELS TECHNIQUE

---

IN the previous Chapter we have seen how SAR sensors allow obtaining all-day all-weather complex reflectivity images of large-scale areas and how, if SAR images are taken at different times, DInSAR techniques allow the exploitation of differential interferograms to retrieve displacement information of affected areas. In this context, the exploitation of the interferometric phase is limited by decorrelation phenomena, as well for the presence of hard atmospheric artifacts. The objective of this Chapter is to provide the reader a general overview of the rationale behind PSI in order to overcome classical DInSAR limitations. All the explanations given in this Chapter focus on the Coherent Pixels Technique, which stands for the PSI technique developed by the RSLab of the UPC used in this PhD Thesis. Finally, some improvements to face landslide monitoring applications are also presented. For the sake of generality all the mathematical developments and explanations given are addressed to space-borne SAR sensors. The adaptation of these techniques for the GB-SAR case is provided in Chapter 6.

## 3.1 Introduction

As seen in the previous Chapter, the exploitation of the interferometric phase is limited by geometrical and temporal decorrelation phenomena. The presence of hard atmospheric artifacts also compromises the applicability of classical DInSAR techniques. In order to overcome these limitations, PSI techniques, which are based on the exploitation of the multi-temporal information contained in a stack of differential interferograms, are employed.

Among the multiple advanced PSI techniques developed by the remote sensing community during the last decade [18–30], the work developed in this PhD Thesis is based on the use of the Coherent Pixels Technique (CPT) [22,176] (implemented in the SubSoft package developed by the RSLab of the UPC). This technique has been widely employed for the monitoring of multiple ground displacement episodes using SAR data collected by space-borne SAR sensors. CPT allows the estimation of the linear and non-linear components of displacement, the topographic error, as well as the atmospheric artifacts from a multi-temporal data set of differential interferograms [22,176].

At present, CPT is divided in four main blocks. The first block is focused on obtaining a selection of differential interferograms and identify a set of persistent scatterers within the AOI in order to minimize the impact of decorrelation phenomena during the following blocks. In this context, a persistent scatterer may be defined as a target that retains its phase quality along the multi-temporal data set of SAR images and can thus be exploited for the retrieval of displacement information. Following this argument, a Persistent Scatterer Candidate (PSC) may be defined as a target selected during the pixel selection step (employing either the coherence stability or the PS criteria) with a high probability of being a persistent scatterer. The Linear Estimation Block (LEB) is devoted to estimate the linear contribution of the differential phase, i.e, the linear component of ground displacement and the residual topographic error component remaining in the differential interferograms. At this stage, the Non-Linear Estimation Block (NLEB) is applied in order to compensate the APS present in the interferograms and provide precise time-series of the displacements produced in the AOI. Finally, the Final Product Layout Block (FPLB) allows the projection of the LOS velocity onto the real ground displacement direction and, moreover, detect and filter-out remaining outliers in the final products.

The explanation of the CPT technique is done chronologically, accordingly to the algorithm's block division described during this introduction.

## 3.2 Interferograms selection and PSCs identification

As seen during the introduction, the interferometric phase quality is a key issue in any PSI processing chain. On the one hand, not all the possible combinations of the interferometric pairs fulfill the phase quality requirements for its later exploitation. On the other hand, interferometric information cannot be exploited from all pixels within the AOI, since only a limited number of them, the persistent scatterers, present the enough phase quality requirements along the multi-temporal data set of SAR images to be included in the PSI processing. In this Section, the methodology followed to filter-out noisy interferograms

is first presented. Then, a complete description of the coherence stability and the PS approaches to the selection of a network of PSCs is put forward. The phase statistics, the estimation accuracy and the relationship between the magnitude of these estimators and the standard deviation of the interferometric phase are widely described. Finally, a new approach to prevent the inclusion of side-lobes when working at full-resolution is proposed. The mathematical formulation provided in this Section is of great importance since it will be the basis for the development of the Temporal Sublook Spectral Correlation (TSSC) pixel selection approach developed in this PhD Thesis (Chapter 7). As it will be shown, this method is devoted to overcome the intrinsic limitations of the classical PSI approaches reviewed in this Section.

### 3.2.1 Selection of differential interferograms

Landslides, which generally occur in natural environments with steep topography, are generally characterized by large temporal and geometrical decorrelation phenomena. Minimizing their negative impact from the beginning of the PSI processing is of great importance in order to achieve a robust network of persistent scatterers. This fact will allow the reliable estimation of displacement maps in a major number of measurement points, which is of great importance in the delineation and characterization of landslides.

In order to minimize the impact of decorrelation phenomena, the selection of interferograms is typically addressed by imposing a maximum limit in the values of temporal and spatial baselines. If an interferometric pair overcomes one of these limits, it is discarded and not included in the later PSI processing.

In this PhD Thesis a slightly different strategy is proposed. The methodology followed is based on the combination of two independent sub-lists. The former is suited for the estimation of displacements, while the latter is optimized for the estimation of the topographic error present in the differential interferograms:

- The sub-list of interferograms for the estimation of displacements is performed by imposing short spatial baselines (to minimize the impact of the topographic error and geometrical decorrelation), but allowing larger temporal ones (to maximize the sensitivity to the displacement phenomena).
- The sub-list of interferograms for the estimation of topographic error is performed by imposing short temporal baselines (to minimize the impact of displacement phenomena and temporal decorrelation), but allowing larger spatial ones (to maximize the sensitivity to the topographic error).

Both lists are finally combined for the joint estimation of the linear displacement and topographic error carried out during the minimization step of the LEB (as it will be explained in Section 3.3.2). With this methodology, the inclusion of interferograms with large values of temporal and spatial baselines is prevented. These pairs are typically noisy due to the presence of both spatial and temporal decorrelation phenomena and, therefore, they are not of practical utility for PSI applications.

Fig. 3.1 shows an example of the selection proposed for the TerraSAR-X data set corresponding to *El Forn de Canillo* (described in Section 1.4 of Chapter 1). Fig. 3.1a shows the total 210 interferometric pairs possible from the 21 TerraSAR-X SAR images

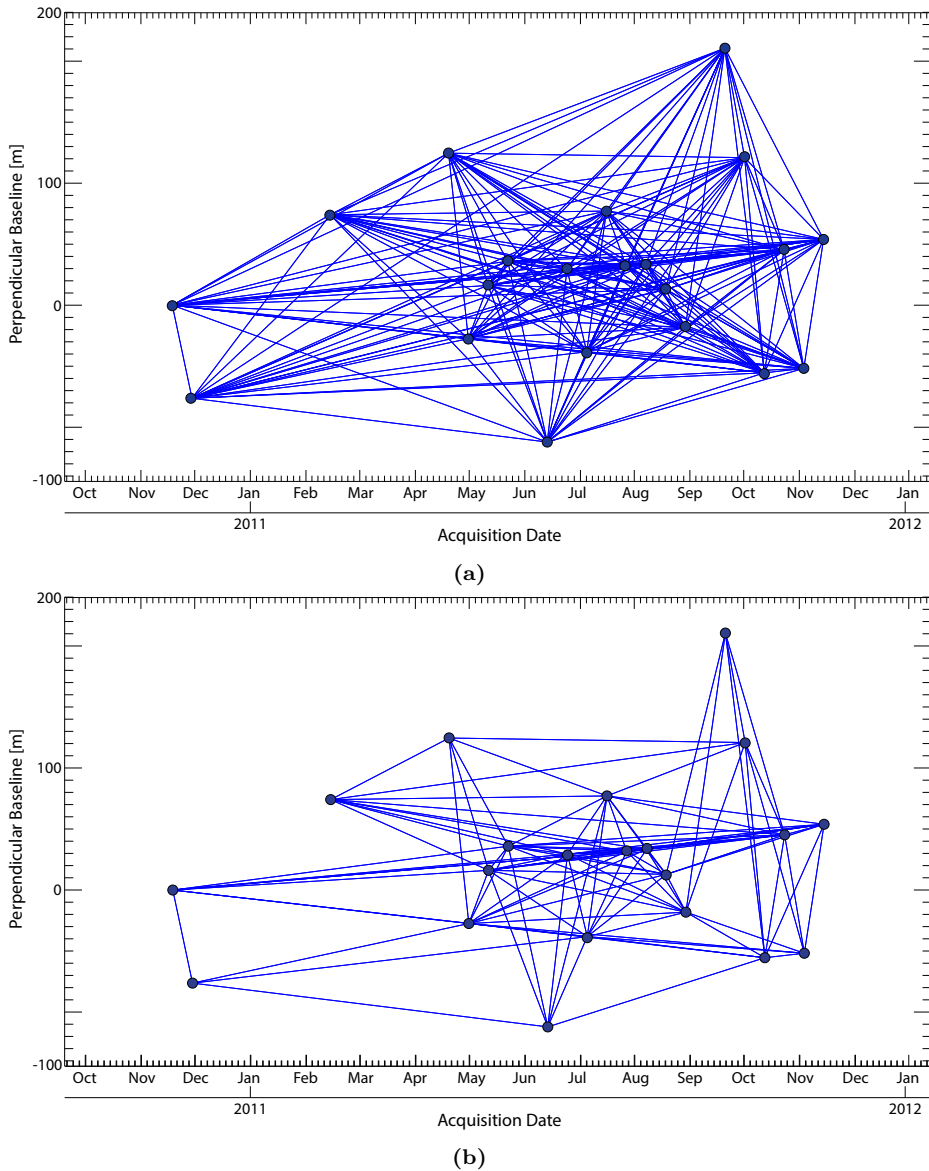


**Figure 3.1:** Interferogram selection for the TerraSAR-X data set corresponding to *El Forno de Canillo*. The arcs linking the points reflect the interconnection between SAR image pairs. (a) Complete list composed by the total 210 interferometric pairs possible from the 21 TerraSAR-X SAR images available. (b) Filtered selection (109 interferograms) by combination of the displacement and the topographic error sub-lists. For the displacement sub-list, 7 months and 60 meters of temporal and spatial baselines have been imposed, respectively. For the topographic error sub-list, 33 days and 200 meters of temporal and spatial baselines have been imposed, respectively.

available. The spatial and temporal baselines of the 210 interferograms is provided in Section G.1 of Appendix G. Fig. 3.1b shows the 109 remaining interferograms after the filtering process described above. For the displacement sub-list, 7 months and 60 meters of temporal and spatial baselines have been fixed, respectively. In parallel, 33 days and 200 meters of temporal and spatial baselines have been fixed to generate the topographic error sub-list. Notice how with this new methodology, interferograms with large values of both temporal and spatial baselines (diagonal pairs in Fig. 3.1a) are not longer selected.

Its worth pointing out that when working with full-resolution PSI methods, point-like scatterers are theoretically not affected by geometrical decorrelation and, for this reason, no restrictions should be applied to the spatial baseline.

### 3.2.2 Coherence stability approach

In this Section, the coherence stability approach for the selection of PSCs is analyzed in detail. The coherence stability criterion is based on the evaluation of the coherence  $\gamma$  [36, 141, 142] seen in Section 2.4 of Chapter 2

$$\gamma = |\gamma| \cdot e^{j\varphi} = \frac{E \{S_1 S_2^*\}}{\sqrt{E \{|S_1|^2\} E \{|S_2|^2\}}} \quad (3.1)$$

The modulus of the complex coherence  $|\gamma|$ , which varies between the range  $[0, 1]$ , indicates the quality of the interferometric phase  $\varphi$ , with the two extremes accounting for the two limit situations of data totally uncorrelated and fully correlated, respectively. Under the assumption of ergodicity and for stationary processes, the expectation operator may be replaced by a spatial average, leading to the maximum likelihood estimator  $\hat{\gamma}$  [143, 144].

$$|\hat{\gamma}(m, n)| = \frac{\left| \sum_{m=0}^{L_1-1} \sum_{n=0}^{L_2-1} S_1(i, j) \cdot S_2^*(i, j) \right|}{\sqrt{\left( \sum_{m=0}^{L_1-1} \sum_{n=0}^{L_2-1} |S_1(i, j)|^2 \right) \left( \sum_{m=0}^{L_1-1} \sum_{n=0}^{L_2-1} |S_2(i, j)|^2 \right)}} \quad (3.2)$$

where  $L_1$  and  $L_2$  refer to the window size in range and azimuth respectively, and  $L = L_1 \times L_2$  indicates the number of looks, i.e., the number of pixels involved in the spatial averaging.

The coherence magnitude thus provides an estimation of the pixel's phase quality for each interferogram, and it is not dependent on the number of images available. For this reason, and contrarily to the PS approach, analyzed in the following Section 3.2.3, a good estimation of the phase standard deviation can be reached even when reduced sets of SAR data ( $\sim 10$ ) are available. Nonetheless, the reliability of the coherence estimator depends on the number of samples involved in the estimation, as seen as follows.

### 3.2.2.1 Estimation Accuracy

In this Section, the mathematical formulation required to evaluate the estimation accuracy and find the relationship between the coherence estimator and the phase statistics is provided. This formulation will be employed to develop the TSSC estimator presented in the Chapter 7 of this PhD Thesis.

Touzi and Lopes demonstrated in [144], that the PDF of the coherence magnitude estimator  $|\hat{\gamma}|$  can be expressed as a function of the true coherence absolute value  $|\gamma|$ , and the number of spatial samples, or looks  $L$ , involved in the estimation as follows

$$pdf(|\hat{\gamma}|; |\gamma|, L) = 2(L-1) \left(1 - |\gamma|^2\right)^L |\hat{\gamma}| \left(1 - |\hat{\gamma}|^2\right)^{L-2} {}_2F_1\left(L, L, 1, |\gamma|^2|\hat{\gamma}|^2\right) \quad (3.3)$$

where the hypergeometric function  ${}_2F_1$  is defined as

$${}_2F_1(a, b, c; z) = \sum_{k=0}^{\infty} \frac{(a)_k (b)_k z^k}{(c)_k k!} \quad (3.4)$$

Through (3.3) the expectation value of the estimated coherence may be derived as

$$E\{|\hat{\gamma}|\} = \frac{\Gamma(L)\Gamma\left(\frac{3}{2}\right)}{\Gamma\left(L + \frac{1}{2}\right)} {}_3F_2\left(\frac{3}{2}, L, L; L + \frac{1}{2}, 1; |\hat{\gamma}|^2\right) \left(1 - |\hat{\gamma}|^2\right)^L \quad (3.5)$$

which is plotted in Fig. 3.2a

Furthermore, the variance of the coherence magnitude estimator may be derived from (3.3) as well

$$\sigma_{|\hat{\gamma}|}^2 = \frac{\Gamma(L)\Gamma(2)}{\Gamma(L+1)} {}_3F_2\left(2, L, L; L+1, 1; |\hat{\gamma}|^2\right) \left(1 - |\hat{\gamma}|^2\right)^L - E\{|\hat{\gamma}|\}^2 \quad (3.6)$$

where the hypergeometric function  ${}_3F_2$  is defined as

$${}_3F_2(a_1, a_2, a_3; b_1, b_2; z) = \sum_{k=0}^{\infty} \frac{(a_1)_k (a_2)_k (a_3)_k z^k}{(b_1)_k (b_2)_k k!} \quad (3.7)$$

and which is plotted in Fig. 3.2b

Finally, the Cramér-Rao bound, which is referred to as a lower bound for the variance may expressed as follows

$$\sigma_{|\hat{\gamma}|, CR}^2 = \frac{\left(1 - |\gamma|^2\right)^2}{2L} \leq \sigma_{|\hat{\gamma}|}^2 \quad (3.8)$$

which is indicated as a reference by the dotted line in Fig. 3.2b

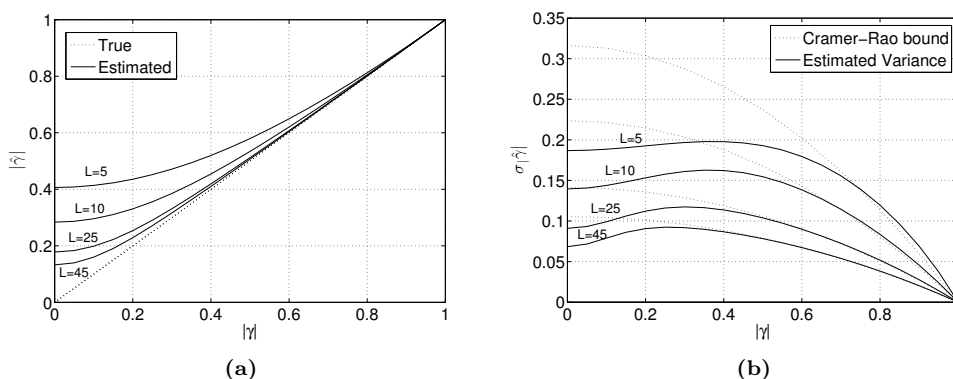


**Figure 3.2:** Coherence magnitude estimator accuracy for different number of looks. (a) Expectation value and (b) standard deviation of the coherence magnitude estimator for different number of looks.

This mathematical development reveals that the coherence magnitude estimator is biased. Its value is overestimated for low magnitudes of true coherence values and/or when a reduced number looks  $L$  is employed during the estimation. Notice how the Cramér-Rao bound represents a good approximation for high coherence values as long as the coherence estimator is unbiased.

In this context, it is interesting to employ a large number of looks to obtain accurate estimations. Nonetheless, this is also translated into a loss of spatial resolution. There is hence a clear trade-off between the estimation accuracy and the spatial resolution difficult to overcome.

Once the accuracy of the estimation has been established, the relationship between the coherence magnitude estimator and the interferometric phase statistics can be discussed. Indeed, this is the key issue to ensure an adequate threshold during the selection of PSCs, and thus obtaining a high-quality network of scatterers within the AOI to carry out a reliable PSI processing.

### 3.2.2.2 Relationship with phase statistics

As indicated in Section 2.1.4 of Chapter 2, assuming a distributed scattering mechanism, the characteristics of a SAR resolution cell may be described by a circular Gaussian distribution. The amplitude is generally characterized by a Rayleigh distribution, whereas the phase has a uniform distribution between the range  $[-\pi, \pi]$ .

Nonetheless, although the PDF of the phase is uniformly distributed between  $[-\pi, \pi]$ , the interferometric phase results of the complex conjugate product of two circular Gaussian signals, which is not necessarily uniform since both have some degree of correlation. Under this formulation, the marginal probability density function of the interferometric phase  $\varphi$  may be expressed as [177, 178]

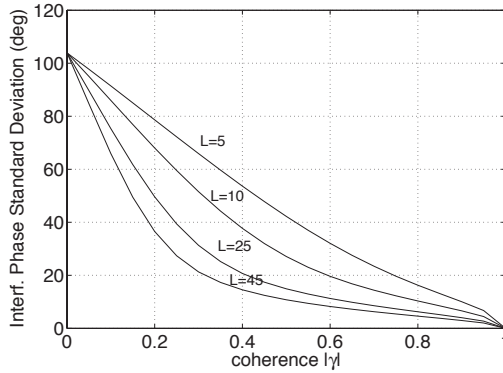


**Figure 3.3:** Standard deviation of the interferometric phase as a function of coherence for different number of looks.

$$pdf(\varphi; \gamma, L, \varphi_0) = \frac{\Gamma(L + \frac{1}{2})(1 - \gamma^2)^L |\gamma| \cos(\varphi - \varphi_0)}{2\sqrt{\pi}\Gamma(L)(1 - \gamma^2 \cos^2(\varphi - \varphi_0))^{L+1/2}} + \frac{(1 - \gamma^2)^L}{2\pi} {}_2F_1(L, 1, ; 1/2; \gamma^2 \cos^2(\varphi - \varphi_0)) \quad (3.9)$$

where  $\varphi_0$  is the expected phase,  ${}_2F_1$  refer to the hypergeometric function defined in (3.4), and  $\Gamma$  accounts for the gamma function defined as

$$\Gamma(L) = \int_0^{\infty} t^{L-1} e^{-t} dt \text{ for } L \in \mathbb{R} \quad (3.10)$$

With the PDF defined in (3.9), the interferometric phase standard deviation can be derived from

$$\sigma_{\varphi} = \sqrt{\int_{-\pi}^{\pi} (\varphi - E\{\varphi\})^2 pdf(\varphi) d\varphi} \quad (3.11)$$

Through numerical simulations from the previous expressions, the phase standard deviation of the interferometric phase may be related with the true coherence magnitude value. Fig. 3.3 shows the result for different ML values. The larger the ML factor employed, the lower the phase standard deviation for the same coherence value, but again it implies an inherent loss of resolution.

For point scatterers, which can be regarded as deterministic signals plus noise, the standard deviation according to (3.11) is overestimated. For those cases, where the coherence is close to 1, the phase standard deviation of the interferometric phase is given by [179]

$$\sigma_{\varphi} = \sqrt{\frac{1 - \gamma^2}{2\gamma^2}} \quad (3.12)$$

Once the relationship between the coherence magnitude estimator metrics and the interferometric phase standard deviation has been described, we are now in position to establish an adequate threshold to ensure a certain phase quality in final PSI products. Nonetheless, some strategy to include temporal sensitivity in the phase statistics estimation still needs to be introduced. This issue is discussed as follows.

### 3.2.2.3 Extension to PSI applications

As stated above, when moving to PSI framework, the temporal axis should be considered in the estimation of the phase statistics. This approach is commonly known as coherence stability criterion and two strategies are the most commonly employed:

- The first approach consists of selecting those pixels exhibiting coherence values above a certain threshold of quality  $\gamma_{th}$  in a certain percentage of the interferograms

$$|\hat{\gamma}| > \gamma_{th} \text{ in a \% of interferograms} \quad (3.13)$$

- The second approach consists of calculating the mean coherence  $|\hat{\gamma}_t|$  along the whole stack of  $M$  interferograms available

$$|\hat{\gamma}_t| = \frac{1}{M} \sum_{i=1}^M |\hat{\gamma}| \quad (3.14)$$

As in the previous case, pixels exhibiting mean coherence values above a certain threshold of quality  $\gamma_{th}$  will be selected as PSCs.

It is worth pointing out that both approaches lead to similar results in terms of pixels' selected. All the results of this PhD Thesis using the coherence stability criterion have been obtained following the latter approach.

## 3.2.3 PS approach

Up to this point, the coherence stability criterion can be employed for the detection of PSCs, especially, in areas with predominance of distributed scatterers. Nonetheless, in presence of high spatial baseline values, or when the employed DEM to obtain the differential interferograms exhibits a limited accuracy, a big amount of differential interferograms turn out to be useless. Moreover, it has been showed how the coherence estimation implies the spatial averaging of data, with its consequent loss of resolution. The larger the window, the higher the estimator accuracy, but also the lower the resolution. When using large ML windows, especially with the new family of high-resolution X-band SAR sensors (as is the case of this PhD Thesis), many stable point-like targets surrounded by non-coherent clutter are unfortunately lost.

In order to overcome these limitations a different strategy is presented in [19], i.e., the PS approach. While the phase is largely affected by different sources of noise (as seen in Section 2.4 of Chapter 2), the amplitude of targets is almost insensitive to most of these phenomena. The rationale behind this approach is to look for those targets exhibiting a

very stable amplitude behavior among long data sets of SAR images. This targets will be related to point-like scatterers and will be theoretically not affected by decorrelation sources.

For this case, the phase stability of targets along the data set is estimated from their temporal amplitude behavior in those pixels exhibiting high SNR values. This concept is developed in the following. Considering a single PDF with a complex reflectivity  $g$ , contaminated by a complex circular Gaussian noise  $n$ , characterized by a power  $\sigma_n^2$  for both the real  $n_r$  and imaginary  $n_i$  components, the distribution of the amplitude values is given by a Rice PDF distribution [19]

$$f_A(a) = \frac{a}{\sigma_n^2} I_0 \left( \frac{a \cdot g}{\sigma_n^2} \right) e^{-\frac{a^2 + g^2}{2\sigma_n^2}} \quad (3.15)$$

where  $I_0$  accounts for the modified Bessel function. For low values of SNR the Rice PDF distribution approaches a Rayleigh only depending on the noise variance  $\sigma_n^2$  (as seen in Section 2.1.4 of Chapter 2), meanwhile, for high values of SNR it can be approximated by a Gaussian distribution. In the latter case, which is a common property of any PS, the following relationship is accomplished

$$\sigma_A \simeq \sigma_{n_r} \simeq \sigma_{n_i} \quad (3.16)$$

Following this argument, the phase dispersion is proportional to the so-called Amplitude Dispersion ( $D_A$ ) [19]

$$D_A = \frac{\sigma_A}{m_A} \quad (3.17)$$

where  $m_A$  and  $\sigma_A$  accounts for the mean and the standard deviation of the temporal amplitude evolution, respectively.

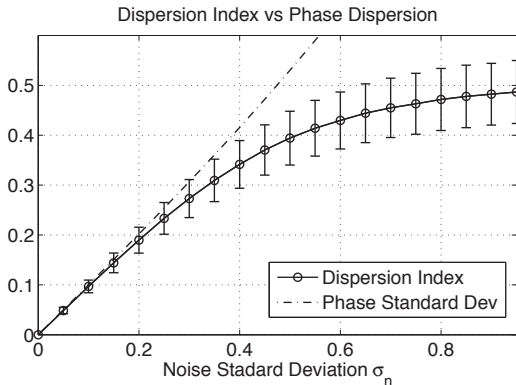
In this framework, PSCs (PSs in this case) are selected evaluating the  $D_A$ , and only those pixels having an amplitude dispersion index under a certain threshold (typically  $D_A < 0.25$ ), will be selected as PSCs.

Fig. 3.4 shows the relationship between the phase standard deviation and the  $D_A$  derived by the numerical simulation stated in [19]. The values of dispersion in the estimation are represented by the vertical bars, while the solid line represents its mean value. The phase standard deviation in radians is represented by the dashed line. We have assumed a set of 30 images and the noise standard deviation,  $\sigma_n$ , has been increased in steps of 0.05 from 0.05 to 0.6. For each value of  $\sigma_n$ , 5000 realizations have been carried out.

If  $\sigma_\phi$  stands for the phase standard deviation of a target in a multi-temporal set of SAR images, and under the hypothesis of two independent normally distributed random variables, the interferometric phase standard deviation  $\sigma_\varphi$  may be expressed as

$$\sigma_\varphi = \sqrt{\sigma_{\phi_1}^2 + \sigma_{\phi_2}^2} \quad (3.18)$$

Finally, it must be pointed out that the quality of the  $D_A$  estimation depends on the number of images available, therefore, a minimum number of images, typically more than



**Figure 3.4:** Comparison of the amplitude dispersion index  $D_A$  and the phase standard deviation (in radians) as a function of noise computed by numerical simulation considering 30 images.

20, is recommended in order to obtain a reliable selection of PSCs. This fact represents the main limitation of the PS approach. There is hence a clear limitation when a full-resolution PSI wants to be performed and the number of SAR images available is reduced.

### 3.2.4 Side-lobe cancellation

SAR systems are inherently band limited in both the range and the azimuth dimensions and, therefore, the PSF has the shape of a bi-dimensional *sinc* function (as seen in Section 2.1.3.3 of Chapter 2). In addition, SAR images are slightly oversampled and, as a consequence, the contribution of a single target extends to more than a single resolution cell. For these reasons, both the main lobe and the side-lobes of high-power scatterers are clearly visible in areas with a low coefficient of back-scattering.

These redundant and ambiguous measurements should be considered when the selection of PSCs is addressed, since the properties of persistent scatterers, for instance amplitude stability for a PS, are generally preserved in both redundant information around the main lobe and side-lobes. If this factor is not taken into account, these undesired artifacts will be erroneously selected as PSCs. This is especially important in PSI strategies based on integrating increments, such as CPT, in which applying a side-lobe mask during the pixel selection step results mandatory in order to avoid the selection of side-lobes. Contrarily, these artifacts may be erroneously selected and propagated as ghost scatterers, thus distorting final PSI products.

Side-lobes are traditionally reduced during the image focusing by applying linear-window filters such as Hanning, Hamming, Kaiser, etc., in the spectral domain. However, the side-lobe reduction (not cancellation) is achieved at the expense of broadening the width of the PSF main lobe and, consequently, losing image resolution.

In this PhD Thesis, a novel use of the SVA algorithm [180] to filter-out all these redundant and ambiguous information, without affecting the quality of SLC images, is proposed. SVA filtering is a nonlinear side-lobe cancellation technique with no loss of im-

age resolution [180]. Its idea is similar to Capon's spectral estimator, but SVA constrains the possible filters to the cosine-on-pedestal family. Unfortunately, applying SVA directly on SAR images can distort the phase information when non-ideal point-like scatterers are present within the AOI. In order to avoid this negative effect, the following methodology is proposed:

- Starting for the first image of the data set, when a side-lobe is detected by the SVA algorithm, its occurrence is stored.
- The process is repeated for all the images of the data set.
- Finally, a map directly related with the number of occurrences along the whole stack is obtained for each pixel through the average of the stored values in the previous steps. This map is addressed as Side Lobe Risk Map (SLRM).

The SLRM can be directly related with the probability of a pixel to be a side-lobe. A side-lobe present in all images will reach the maximum value of one in the SLRM, meanwhile, those pixels with zero value in the SLRM will have no risk of being a side-lobe. This information is finally employed to derive a binary mask which should be directly applied to the network of PSCs selected in order to prevent the inclusion of side-lobes in the latter PSI processing.

In Fig. 3.5 the SLRM over a TerraSAR-X image corresponding to *El Forn de Canillo* is depicted. Fig. 3.5a shows the reflectivity of an area with man-made structures producing clearly visible side-lobes. Fig. 3.5b shows the SLRM over the selected area. Notice that high values of SLRM are related to side-lobes and to ambiguous information around the main-lobe in the image. These pixels should be filtered-out prior to the application of any PSI algorithm.

In Appendix C, a more complete description and analysis of the SVA technique is put forward. Moreover, a demonstration of how applying this filter directly over SAR images can corrupt its amplitude and phase information, as stated above, is put forward.

### 3.2.5 Selection of PSCs over El Forn de Canillo test site

This Section presents the selection of PSCs over the landslide of *El Forn de Canillo* employing the TerraSAR-X data set described in Section 1.4 of Chapter 1.

Fig. 3.6 illustrates the mean coherence (see Fig. 3.6b) and  $D_A$  (see Fig. 3.6c) for the AOI. As seen, *El Forn de Canillo* is mainly a vegetated area only containing few man-made structures and rocky areas suitable for the PSI processing. In general, the highest quality points detected from both estimators, i.e, high mean coherence or low  $D_A$ , correspond with these areas. Notice how both estimators follow the road, the buildings, and the rocky and bare surfaces present in the scenario. Despite this, Fig. 3.6b evidences the loss of spatial resolution when employing the mean coherence approach (a  $5 \times 5$  ML factor for this example).

This fact is more noticeable in Fig. 3.7. Fig. 3.7a and Fig. 3.7b show a comparison in terms of pixels' selected between the coherence stability approach and the PS technique, respectively. In order to ensure a fair comparison, equivalent thresholds over the phase quality estimators have been established to provide the same requirements in terms of interferometric phase standard deviation. A threshold of 0.65 considering a  $5 \times 5$  ML

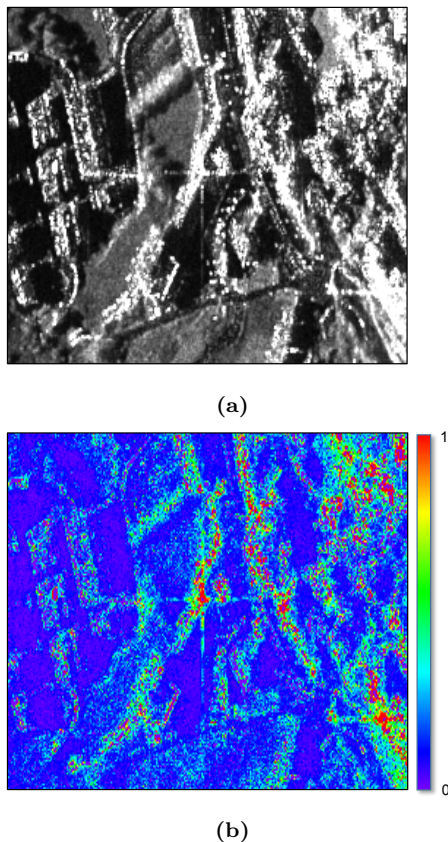


**Figure 3.5:** SLRM over a TerraSAR-X image corresponding to *El Forn de Canillo*. (a) Reflectivity image of an area with man-made structures producing clearly visible side-lobes. (b) SLRM over the selected area.

(see Fig. 3.3) has been fixed to the mean coherence and, in parallel, a threshold of 0.2 has been applied to the  $D_A$  (see Fig. 3.4) in order to produce the same response in terms of interferometric phase standard deviation ( $15^\circ$  for these thresholds). Notice that the phase standard deviation value is given at interferogram level and, for this reason, in the amplitude dispersion case the phase standard deviation, which is given at image level, has to be multiplied by  $\sqrt{2}$  according to (3.18). This is  $11^\circ$  in order to provide a interferometric phase standard deviation of  $15^\circ$ .

As seen in the analysis of the estimators showed previously, both selections of PSCs are concentrated in the road, the buildings, and the rocky and bare surfaces present in the AOI. Notice how the degradation of spatial resolution is more evident here. This fact leads to a significant loss of pixels (5 times less) and details in the final PSI results, as it will be shown in Section 3.3.4.

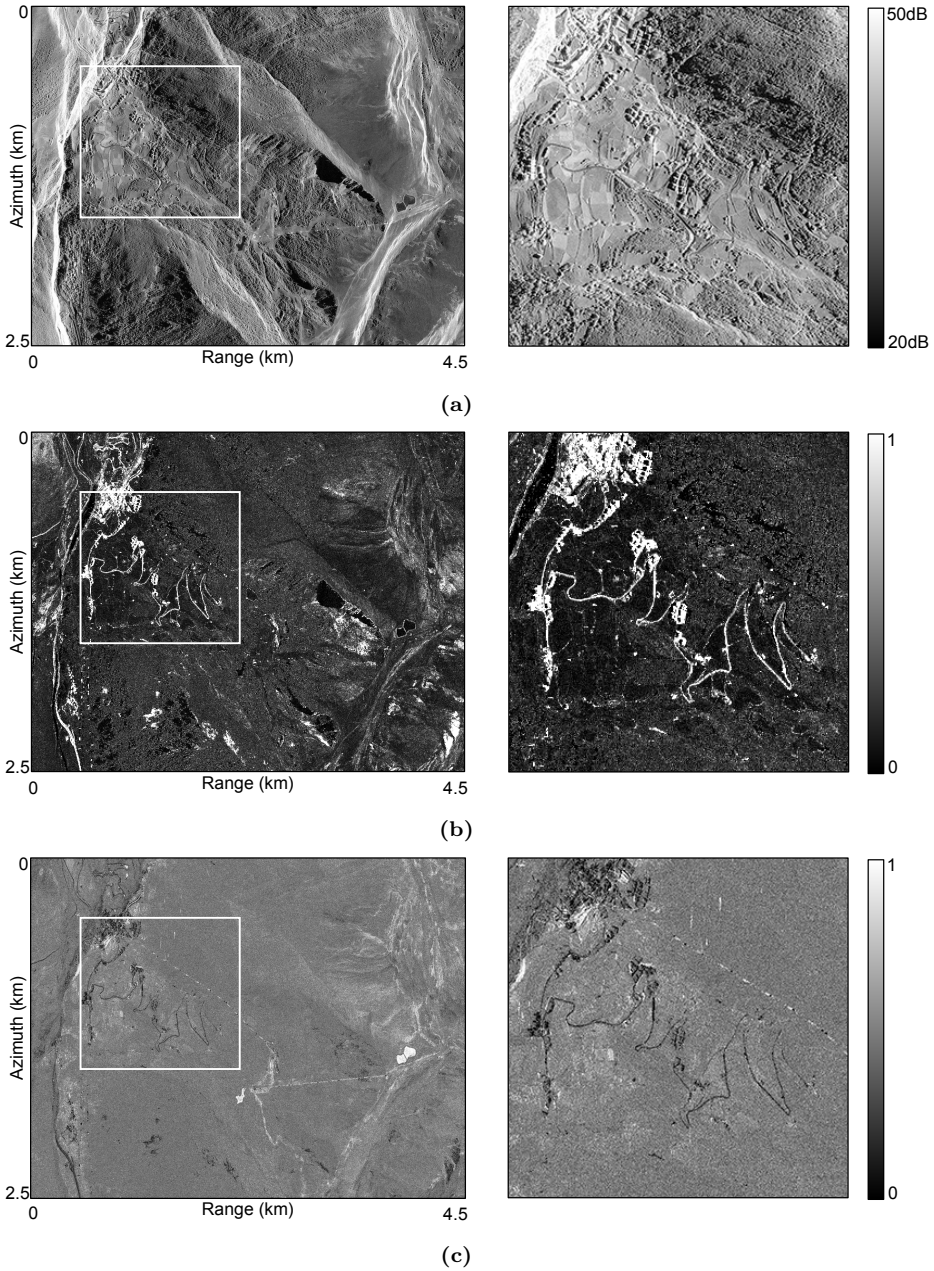


**Figure 3.6:** Mean coherence and  $D_A$  maps over the TerraSAR-X data set corresponding to *El Forn de Canillo*. (a) Amplitude in dB of a SAR image collected by the TerraSAR-X sensor in sliding-spotlight mode. (b) Mean coherence and (c)  $D_A$  map of the AOI. The figures on the right represent a zoom of the area highlighted with a white rectangle in the figures on the left.

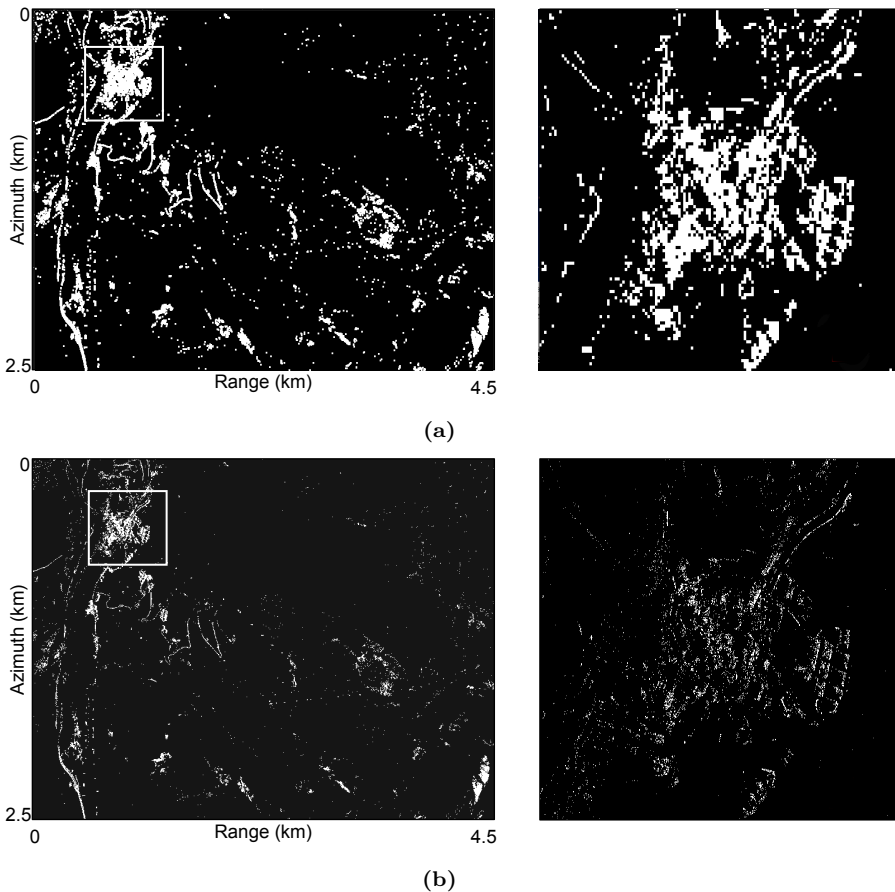


**Figure 3.7:** PSCs selected by means of (a) mean coherence and (b)  $D_A$  maps over the TerraSAR-X data set corresponding to *El Forno de Canillo*. The figures on the right represent a zoom of the area highlighted with a white rectangle in the figures on the left.

### 3.3 Linear Estimation Block

The objective of the LEB of CPT is to estimate the linear components of the differential phase, these are the linear component of ground displacement and the residual topographic error component due to inaccuracies in the DEM employed during the generation of differential interferograms. The inputs correspond to a selection of differential interferograms and a map of PSCs obtained during the previous step.

The LEB may be divided in the following sub-blocks:

- **Triangulation.** It is used to work with phase increments between pixels, instead of absolute phases. The objective of this approach is threefold. On the one hand, atmospheric artifacts are minimized since they change smoothly in space. On the other hand, the different phase offsets between interferograms are canceled. Finally, assuming a high density of pixel candidates, the phase increments will be in most

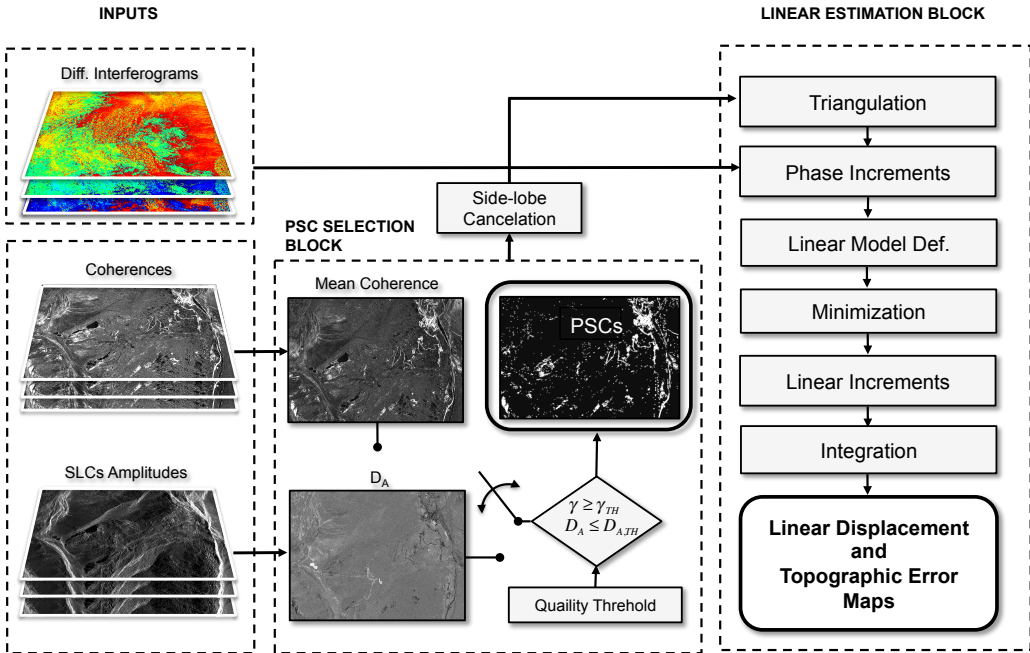


Figure 3.8: LEB layout of CPT.

cases lower than  $\pi$  radians and, therefore, an unwrapping process is not necessary at this stage.

- **Minimization.** In order to estimate the linear displacement rate and the residual topographic components of the interferometric phase, a linear model including only these elements is defined for each arc of the triangulation. Then, the model is adjusted to the data through the minimization of a cost function. At the end of this step, an increment of linear displacement rate and topographic error are obtained for each arc of the network performed in the previous step.
- **Integration.** At this point, the absolute values of linear displacement and topographic error for each PSC are obtained through an integration process (from the increments obtained in the previous step), using one or multiple seeds with known behavior as tie points.

The LEB flow-chart is depicted in Fig. 3.8.

### 3.3.1 Triangulation

The floating information contained in the interferograms due to the presence of different phase offsets among them causes the absolute phase of individual pixels to be not of practical utility. A possible solution consists of performing a phase calibration process employing coherent stable areas free of any displacement process, but also not affected by atmospheric artifacts. This solution results difficult to be implemented in the practice

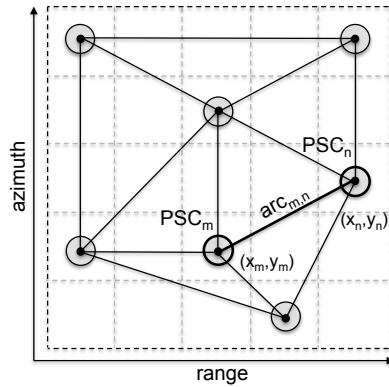


**Figure 3.9:** Example of Delaunay triangulation.

since, on the one hand, *a priori* information about the displacement phenomena is required and, on the other hand, atmospheric artifacts are random signals difficult to characterize.

This problem is overcome in CPT carrying out a Delaunay triangulation [181]. This type of triangulation relates pixels of an irregular network of PSCs generating non-overlapped triangles, as shown in Fig. 3.9. The objective of this triangulation is to work with phase increments among pixels instead of absolute phases, thus canceling the offset problem between interferograms for multi-temporal studies. Other benefits are obtained using this strategy. Since APS change smoothly in space (the correlation window of the atmosphere is typically around 1 km), atmospheric artifacts (as well orbital ones) are minimized thanks to the triangulation. In order to fulfill these requirements, the maximum length allowed to connect PSCs is typically set to 500-750 meters. Finally, this step is also important to avoid the phase unwrapping at this stage. Assuming a high density of PSCs the phase increments may reasonably be supposed to have values lower than  $\pi$  radians in most of the differential interferograms. As it will be detailed later, the model adjustment is not affected by having wrapped phases in some of the interferograms and, therefore, the phase unwrapping step can be skipped at this point.

It is worth pointing out that when some areas do not have the required density or different clusters of pixels appear, which is the case of the natural environment of *El Forn de Canillo*, redundant network strategies may be employed. In this PhD Thesis this solution has been implemented.

The rationale is based on connecting PSCs uniformly in all directions up to a maximum number of arcs forming a spider web-like network which will add redundancy during the integration step, which is explained in Section 3.3.3.

Fig. 3.10 illustrates the difference between a Delaunay and a spider web-like network over the TerraSAR-X data set corresponding to *El Forn de Canillo*. For the spider web-like network case, a maximum number of 5 connections up to a maximum distance of 750 meters has been established.

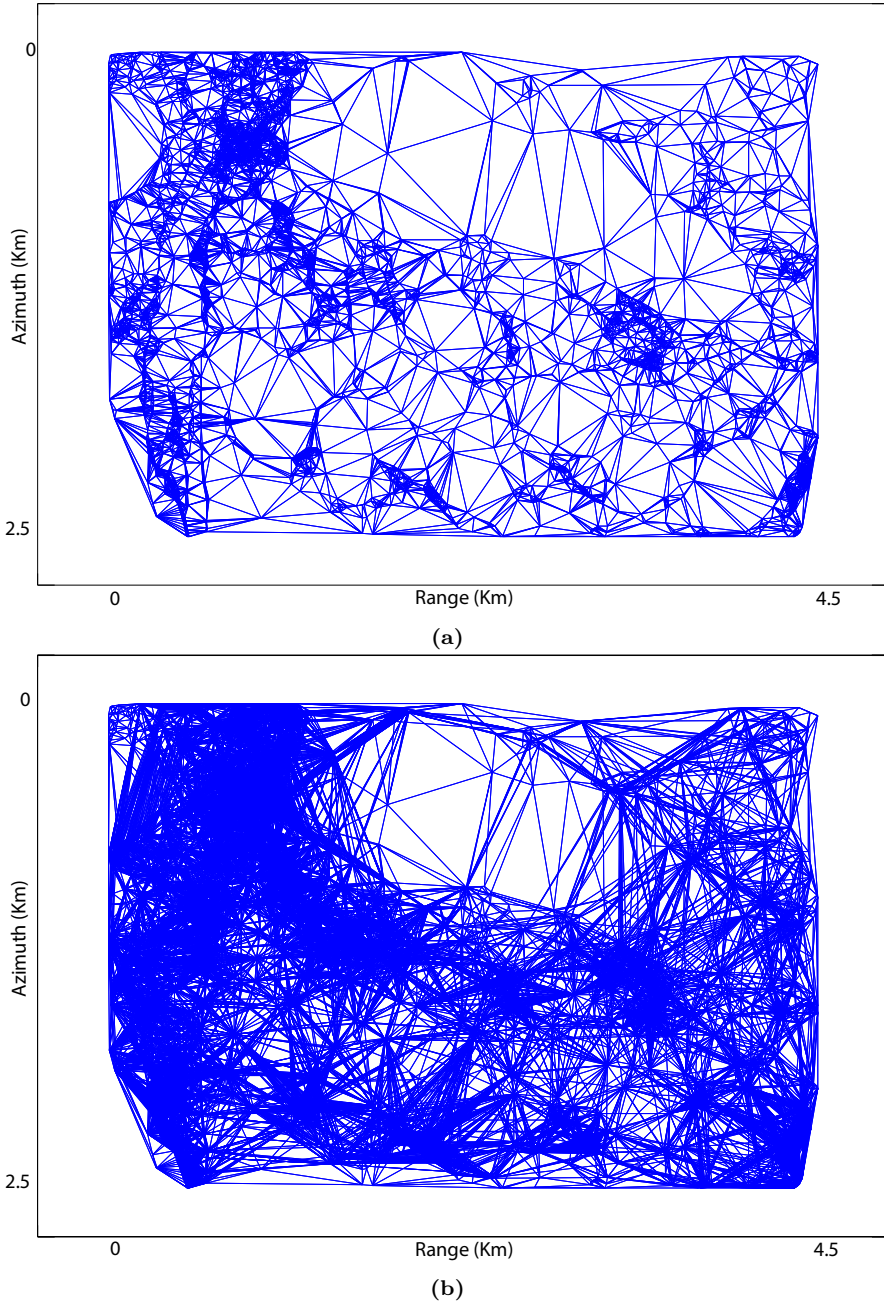


**Figure 3.10:** (a) Delaunay and (b) spider web-like network for the TerraSAR-X data set corresponding to *El Forn de Canillo*. For the spider web-like network case, a maximum number of 5 connections up to maximum distance of 700 meters has been established.

### 3.3.2 Minimization

Once the triangulation is carried out, a set of  $N_{rel}$  arcs or links between neighboring PSCs is obtained. At this stage, the interferometric phase increment for an arc of the  $i$ -th differential interferogram  $\Delta\varphi^i$  between two PSCs connected by the triangulation ( $PSC_m$  and  $PSC_n$ ), can be expressed as the contribution of the following terms [22, 176]

$$\begin{aligned}\Delta\varphi_i(T_i, B_{n,i}, x_m, y_m, x_n, y_n) &= \Delta\varphi^i(T_i, B_{n,i}, arc_{m,n}) \\ &= \frac{4\pi}{\lambda} \cdot T_i \cdot (v(x_m, y_m) - v(x_n, y_n)) \\ &+ \frac{4\pi}{\lambda} \cdot \frac{B_{n,i}}{R_i \sin \theta_i} \cdot (\varepsilon(x_m, y_m) - \varepsilon(x_n, y_n)) \\ &+ \Delta\varphi_i^{res}\end{aligned}\quad (3.19)$$

where  $(x_m, y_m)$  and  $(x_n, y_n)$  indicate the coordinates of the nodes forming the  $arc_{m,n}$ ,  $v(x_m, y_m) - v(x_n, y_n)$  and  $\varepsilon(x_m, y_m) - \varepsilon(x_n, y_n)$  refer to the increment of linear displacement rate and topographic error, respectively,  $\lambda$  indicates the wavelength,  $T_i$  and  $B_i$  are the temporal and spatial baselines, respectively,  $R_i$  is the sensor to target distance,  $\theta_i$  the incidence angle, and  $\Delta\varphi_i^{res}$  account for the atmospheric artifacts  $\beta_i$ , the non-linear displacement  $\eta_i$  and the noise  $n_i$  components

$$\begin{aligned}\Delta\varphi_i^{res}(arc_{m,n}) &= (\beta_i(x_m, y_m) - \beta_i(x_n, y_n)) \\ &+ (\eta_i(x_m, y_m) - \eta_i(x_n, y_n)) \\ &+ (n_i(x_m, y_m) - n_i(x_n, y_n))\end{aligned}\quad (3.20)$$

At this point, a linear model  $\Delta\varphi_i^{model}$  may be defined for each arc of the triangulation in order to estimate the linear displacement rate and the topographic error increments as follows

$$\Delta\varphi_i^{model}(T_i, B_{n,i}, arc_{m,n}) = \frac{4\pi}{\lambda} \cdot T_i \cdot \Delta v(arc_{m,n}) + \frac{4\pi}{\lambda} \cdot \frac{B_{n,i}}{R_i \sin \theta_i} \cdot \Delta\varepsilon(arc_{m,n}) \quad (3.21)$$

where  $\Delta v = v(x_m, y_m) - v(x_n, y_n)$  refers to the increment of linear displacement rate and  $\Delta\varepsilon = \varepsilon(x_m, y_m) - \varepsilon(x_n, y_n)$  to the increment of topographic error.

Since the increments of linear velocity and topographic error are constant for each node (and arc) in the whole set of differential interferograms, it is possible to obtain a good estimation of them by adjusting the linear phase model  $\Delta\varphi_i^{model}$  (defined in (3.21)) to the observations  $\Delta\varphi^i$  (defined in (3.19)). Finally, it is worth pointing out that the remaining atmospheric artifacts in those links characterized by longer distances (recall that the shorter the distance, the lower the atmospheric phase component), will behave as random signals along the temporal axis and, therefore, they will not fit the linear model.

Following this argument, the defined model is adjusted to the data observations through the minimization of a cost function  $\Gamma$ , defined in the complex plane, and addressed as Model Adjustment Function (MAF) [22, 176]

$$\Gamma(arc_{m,n}) = \frac{1}{N_{\text{int}}} \cdot \sum_{i=1}^{N_{\text{int}}} \left| e^{-j\Delta\varphi_i(T_i, B_{n,i}, arc_{m,n})} - e^{-j\Delta\varphi_i^{\text{model}}(T_i, B_{n,i}, arc_{m,n})} \right|^2, \quad (3.22)$$

that can be rewritten as

$$\Gamma(arc_{m,n}) = 2 \cdot \left( 1 - \frac{1}{N_{\text{int}}} \cdot \sum_{i=1}^{N_{\text{int}}} \text{Re} \left\{ e^{-j(\Delta\varphi_i(T_i, B_{n,i}, arc_{m,n}) - \Delta\varphi_i^{\text{model}}(T_i, B_{n,i}, arc_{m,n}))} \right\} \right), \quad (3.23)$$

which is computationally more efficient, giving exactly the same solutions.

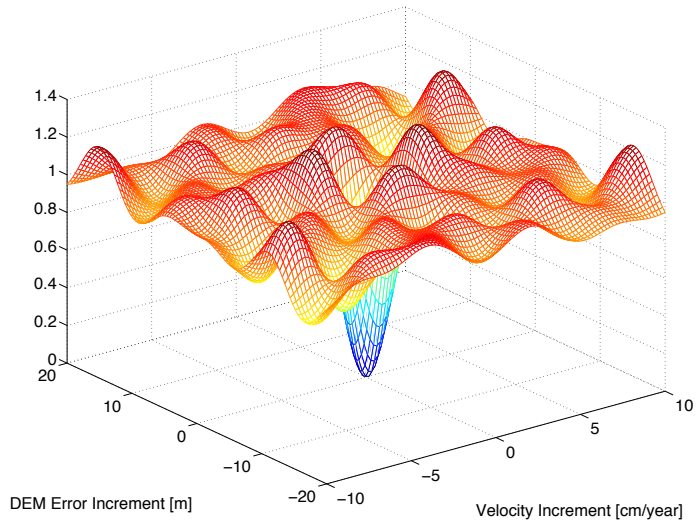
In conclusion, the objective of this step is to adjust the linear phase model to the observations (interferometric phases) in order to find the optimal values of  $\{\Delta v, \Delta\varepsilon\}$  that make the cost function  $\Gamma$  tend to zero. Since the model adjustment is performed in the complex plane, with a good distribution of temporal and spatial baselines it is possible to deal with wrapped phases.

The CPT solves this minimization problem using the Conjugate Gradient Method (CGM) method [182]. This approach increases both the accuracy and the processing speed with respect to the brute force technique, in which a set of test parameters are evaluated in order to search the minimum of  $\Gamma$ . Further information about the CGM minimization is provided in Section E.2 of Appendix E.

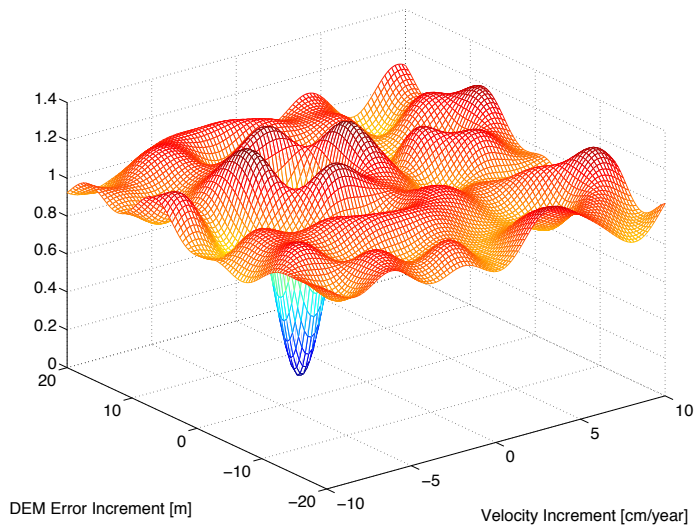
Fig. 3.11 illustrates the shape of the MAF around its minimum value along the  $\{\Delta v, \Delta\varepsilon\}$  axis for a simulated scenario free of noise composed by 109 interferograms uniformly distributed in terms of both temporal (between 11 and 365 days) and spatial (between  $-500$  and  $500$  meters) baselines.  $R$ ,  $\theta$ ,  $\lambda$  and the revisiting time have been defined according to TerraSAR-X setting parameters. Fig. 3.11a and Fig. 3.11b shows the response of a link with  $\{0 \text{ cm/y}, 0 \text{ m}\}$  and with  $\{-2 \text{ cm/y}, 5 \text{ m}\}$  of linear velocity and topographic error increments, respectively. Notice how the minimum is clearly visible for both cases and how the pair of linear increments have been perfectly estimated.

Some considerations about the MAF should be briefly discussed at this point:

- On the one hand, it must be taken into account that the MAF is sensitive to the distribution of spatial and temporal baselines. Concretely, the temporal and spatial sampling of baselines is related with the accuracy in the estimation of the linear parameters. The maximum value of spatial and temporal baseline will characterize the width of the valley around the minimum for the topographic error and the linear displacement increment dimension, respectively. In this framework, distributions characterized by larger baseline limits will result in narrower valleys, thus leading to a better estimation of the linear parameters. Contrarily, increasing these limits lead to major decorrelation phenomena (as seen in Section 3.2.1), thus introducing noise in the minimization step. There is hence a clear trade-off between these two aspects. Finally, notice that in the limit situation of having a zero-baseline distribution, which in fact corresponds to the GB-SAR case, the MAF function only will have a minimum in the velocity increment dimension. For that case, the problem becomes uni-dimensional, as it will be shown during the description of the GB-SAR PSI chain in Chapter 6.



(a)



(b)

**Figure 3.11:** MAF of different links for a simulated scenario free of noise composed by 109 interferograms uniformly distributed in terms of both temporal (between 11 and 365 days) and spatial (between  $-500$  and  $500$  meters) baselines. (a) Linear velocity increment:  $0$  cm/year. Topographic error increment:  $0$  meters. (b) Linear velocity increment:  $-2$  cm/year. Topographic error increment:  $5$  meters.

- On the other hand, since the MAF function can be seen as a normalized sum of 2D sinusoidal functions at different frequencies, the presence of ambiguities for the linear displacement increment case should be considered. Defining the minimum temporal baseline difference as  $\Delta T_{\min}$ , the distance between ambiguities is given by the following expression

$$\Delta v_{amb} = \frac{\lambda}{2 \cdot \Delta T_{\min}} \quad (3.24)$$

The search margin during the minimization must hence be set taking into account this aspect in order to avoid the presence of ambiguities.

These considerations aforementioned are explained in further detail in Appendix D.

Once the model adjustment is performed, the result is a set of velocities and topographic error increments for each arc of the triangulation  $\{\Delta v, \Delta \varepsilon\}$  and the integration step can be carried out.

### 3.3.3 Integration

At the end of the last block, the values of  $\{\Delta v, \Delta \varepsilon\}$  have been obtained for each arc of the triangulation. Now the absolute values of velocity  $v$  and topographic error  $\varepsilon$  for each pixel can be estimated through an integration process. As the solution is floating, one or multiple seeds, with known velocity and topographic error values, should be used as tie points during this process [22, 176]. Errors locating the seeds can introduce offsets in final results.

As seen in the previous Section, the minimization of  $\Gamma$  always provides a pair of velocities and topographic error values regardless of the quality of the adjustment. Unfortunately, several factors affect the performance of the minimization process. For this reason, prior to the integration, the quality of the solutions should be evaluated in order to discard incorrect solutions. With that purpose, the model coherence  $\gamma_{\text{mod}}$  is defined

$$\gamma_{\text{mod}}(arc_{m,n}) = \frac{1}{N_{\text{int}}} \cdot \left| \sum_{i=1}^{N_{\text{int}}} e^{-j(\Delta \varphi_i(T_i, B_{n,i}, arc_{m,n}) - \Delta \varphi_i^{\text{model}}(T_i, B_{n,i}, arc_{m,n}))} \right| \quad (3.25)$$

Notice that the model coherence lies inside the interval  $[0, 1]$ . It reaches the maximum value when the linear model perfectly fits the data, and tends to zero in presence of a poor model adjustment. This is mainly produced in those links affected by the following artifacts:

- **Noisy PSCs.** As seen in Section 3.2 not all the pixels within the interferogram are of practical utility since, mainly due to decorrelation phenomena, only a limited number of them fulfill the phase quality requirements to the later application of PSI techniques. In this context, an adequate threshold must be set in order to satisfy an interferometric phase standard deviation of around 15 – 20 degrees.
- **Non-linearities.** Since this block is based on a linear model assumption, any non-linear displacement contribution worsens the estimation of the linear parameters.

- **Atmospheric artifacts.** The presence of hard atmospheric artifacts degrades the model coherence. In this case, it is advisable to densify as much as possible the network of PSCs to improve the grid's density, and minimize the distance between neighboring PSCs forming an arc.

In conclusion, mainly due to the presence of non-linearities and APS, not all the links minimized present the same quality. For this reason, prior to the integration process, a pre-filtering step is typically addressed in order to include in the integration only those links presenting a certain threshold of quality. Specifically, those arcs presenting values of  $\gamma_{\text{mod}}$  lower than a certain threshold of model coherence will be rejected and not taken into account during the integration. Isolated pixels will be also removed at this stage.

As done during the selection of PSCs, a threshold of model coherence is hence fixed in order to ensure a certain value of phase standard deviation in the integrated results. Unfortunately, the problem here become more complex. In order to face the possibility of having non-linear displacement terms in some phase increments, which degrades the model coherence, thresholds are usually relaxed. This is to prevent the risk of removing some useful arcs due to non-linearities. Contrarily, it is interesting to ensure an adequate threshold to remove those connections affected by hard atmospheric artifacts. The objective is to prevent the inclusion of atmospheric patterns in the final displacement results. Finally, it is important to reach a trade-off between filtering low-quality arcs and keep the network dense and well-connected. The idea is that if some specific link is bad estimated, other links can help during the retrieval of the correct values of linear velocity and topographic error. If different clusters are created during the pre-filtering step it is important to set one or more seeds in each cluster. All the disconnected clusters without seeds will be removed prior to the integration process.

The model coherence threshold is typically fixed around 0.5 but, as mentioned above, it depends on the specific characteristics of the AOI and data set (land cover, distribution of temporal and spatial baselines, number of images, characteristics of the displacement, etc.). For the test site of *El Forn de Canillo*, a model coherence threshold of 0.4 was finally selected in order to fulfill all the requirements described above.

Once the pre-filtering is carried out, the integration process can be performed. The CPT can work with path-based integration methods, such as RG [134], or with global-based ones, such as CGM [182].

RG integration method departs from one or several reference points characterized by high-quality relationships in terms of model coherence (typically above 0.9), which are called seeds. From these points, all the paths covering the PSCs are extended through the relationships, weighting each relationship by its model coherence value. This technique presents two main drawbacks, it is path dependent, which leads to an integration solution with a certain dependency on the distance from the seeds, i.e, with large propagation errors and, on the other side, it presents a slow performance over large-scale areas of observation.

For these reasons, global integration methods, which seek for global solutions path-independent, are typically employed. The CPT employs a solution based on the CGM algorithm. This solution is based on the minimization of the global residue for all the integrated values, thus providing more robustness and a better response in terms of computation time compared with the RG. CGM is one of the most employed iterative methods

for solving systems of linear equations of the form

$$\mathbf{Ax} = \mathbf{b} \tag{3.26}$$

which is precisely the objective here.

If  $m$  accounts for the number of relationships and  $n$  for the number of PSCs, the following matrices can be defined:

- $\mathbf{W}$ . A  $m \times n$  square diagonal matrix containing the model coherence of each arc, which allows to reduce the impact of low quality links during the integration.
- $\mathbf{A}$ . A  $m \times n$  matrix defining the relationships.
- $\mathbf{x}$ . A vector of  $n$  elements with the unknowns representing either the absolute value of linear velocity or topographic error.
- $\Delta\mathbf{y}$ . A vector of  $m$  elements containing the linear parameter increments of the relationships  $\{\Delta v, \Delta \varepsilon\}$ .

Under these definitions, the system of equations to solve may be expressed as follows

$$\mathbf{WAx} = \mathbf{W}\Delta\mathbf{y} \tag{3.27}$$

If  $\mathbf{C} = \mathbf{WA}$  and  $\Delta\mathbf{y}' = \mathbf{W}\Delta\mathbf{y}$  the resulting system of equations is equivalent to (3.26) and, therefore, it can be solved by means of CGM. Further information about how the CGM is used during the integration step is provided in Section E.3 of Appendix E.

Once the absolute values of velocity and topographic error are obtained, an integration test is carried out in order to evaluate the errors which may have occurred during the integration. The objective of this step is to compare the increments calculated from the integrated values with the increments computed during the minimization step. Those links with major deviation are discarded. With that purpose in mind, a maximum threshold value of difference is fixed (typically a factor of 2 or 3 of the Root Mean Square Error (RMSE) value), and those relationships overcoming this established threshold are removed. If a pixel goes out of relationships is also discarded. After this filtering step, the integration process with the surviving relationships and pixels is performed again.

Finally, since the accuracy of the linear displacement strongly depends on the density and quality of the selected pixels, the CPT algorithm includes a multi-layer processing in order to improve the linear estimation block [176]. This method is based on dividing the selected pixels in different layers according to their phase quality. Beginning with the top layer, the linear block is iteratively processed by adding successive low-quality layers. Once the absolute velocity values are obtained from a layer, they are fixed and used as seeds in the following integration processes. With this approach, the density of pixels is largely improved but the quality of the PSI results for the best pixels is not affected by the low quality ones [176].

### 3.3.4 Linear estimation over El Forn de Canillo test site

To conclude this Section, the linear results for the TerraSAR-X data set corresponding to *El Forn de Canillo* are presented to show the goodness of the techniques proposed.

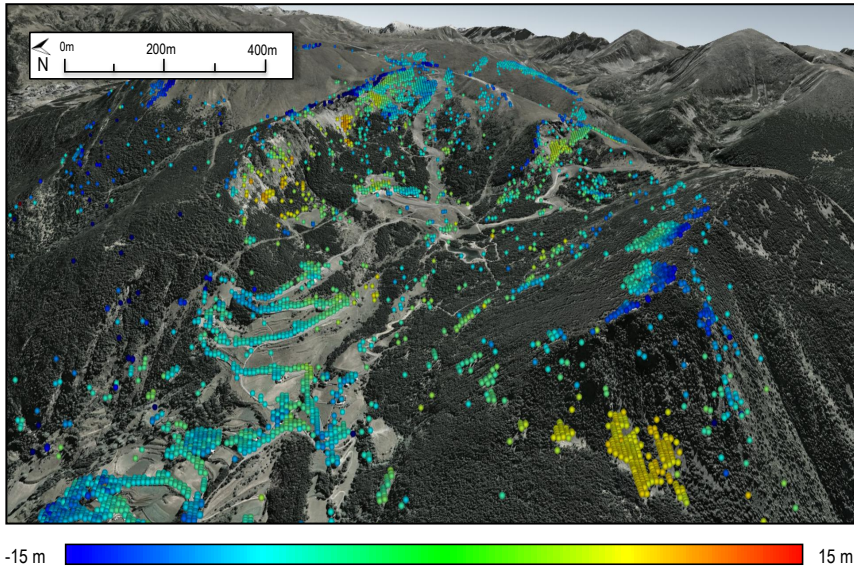
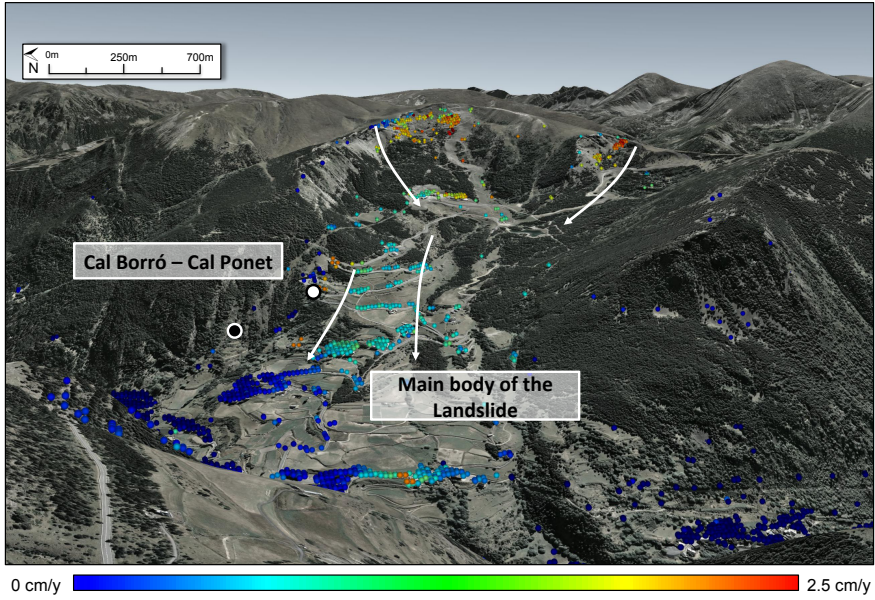


**Figure 3.12:** Geocoded topographic error for the TerraSAR-X data set corresponding to *El Forn de Canillo* using the  $D_A$  approach.

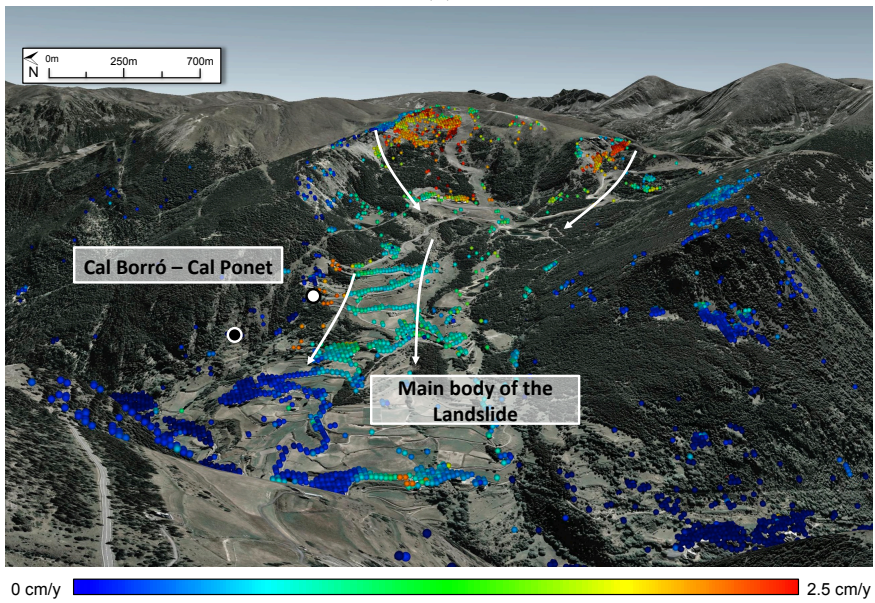
Fig. 3.12 shows the topographic error retrieved in the upper part of the landslide. As expected, the magnitude is higher in areas with steep topography. The DEM model employed in this PhD Thesis to compensate the topographic component of the interferograms corresponds to a SRTM with 90 meters of resolution. The topographic error map retrieved during the LEB has been employed in the geocoding of the final PSI products (to update the heights of the SRTM DEM), with the objective of improving the accuracy during the geo-localization process.

Fig. 3.13 shows the linear displacement in the LOS obtained with the coherence stability technique (Fig. 3.13a) and the PS approach (Fig. 3.13b). Results have been geocoded over a Google Earth image. For the coherence stability a threshold of 0.65 has been employed. The PS technique has been carried out using a  $D_A$  threshold of 0.2. These thresholds are set in order to ensure the use of pixels with similar interferometric phase standard deviation ( $15^\circ$ ) in both cases, as seen in Section 3.2.5.

First of all, notice the high agreement between the displacement results obtained with the different PSI approaches. As expected, PS and coherence stability results are retrieving similar displacement trends, except for the increase in pixel density (five times more in the latter), especially, over those areas with exposed rocks surrounded by vegetation (which may be appreciated at both sides of the landslide). As seen during the pixel selection block, the ML carried out in the coherence stability approach limits the selection of deterministic point-like scatterers surrounded by non-coherent clutter. Indeed, the denser results benefit the construction of a more robust network during the minimization and integration processes of the CPT, thus improving the reliability of PSI results, but also favoring the delineation and characterization of the landslide. Finally, notice that the displacement magnitudes obtained by means of the PS approach reach slightly higher values



(a)



(b)

**Figure 3.13:** Linear displacement for the TerraSAR-X data set corresponding to *El Forn de Canillo* in the LOS using (a) the coherence stability technique and (b) the PS approach. The black spot indicates the location of the seed employed during the integration step. The white spot indicates the location of the inclinometer *S10*, which will be employed as ground truth to validate the results.

of displacements (two or three millimeters more) compared with the coherence stability results. This difference may be produced by the ML carried out during the coherence estimation, which leads to an averaging of the displacement within the multi-looked area.

Regarding the interpretation of the results, notice how in the lower part of the landslide the PSI results obtained show a complete agreement with the conclusions extracted from the field monitoring campaigns presented in Section 1.4 of Chapter 1. Concretely, the displacement maps obtained reveal that the main body of the landslide experienced a residual movement of 1 cm in the LOS during the monitoring period. In addition, the local slide of *Cal Borró-Cal Ponet* may be perfectly identified, presenting a higher activity of roughly 2 cm/year in the LOS.

Furthermore, some displacement trends, unknown until now, have been also identified in the upper part of the *El Forn de Canillo*: the crest linking the *Pic del Maïans* to the *Pic d'Encampadana* and another closer to the area known as *Pla del Géspit*. Some field inspections (reviewed in Section 1.4 of Chapter 1) reveal the existence of displacement indicators such as structural disturbances, tension cracks, depressions filled with sediments, as well as tilted and rotated blocks with weathered surfaces. Finally, it is worth pointing out that all the displacements showed are referred to the LOS. In Section 3.5, the way to re-project these displacement values onto the real ground displacement direction in order to make a quantitative comparison with the ground truth available, will be described

Thanks to the improved resolution characteristics of the sliding-spotlight TerraSAR-X imaging mode, a full-resolution PSI has been possible in the challenging environment of *El Forn de Canillo*. A large amount of nice details and an unprecedented quantity of measurements are noticeable in the displacement results, especially, when working at full-resolution with the PS approach. Before the arrival of this new generation of SAR sensors, this kind of processing was not possible. It has thus been demonstrated that when the number of SAR images is adequate (more than 20) a reliable full-resolution PSI can be performed through the  $D_A$  estimator, even over natural environments. The following Chapters are addressed to compare these results with the ones obtained with the RikSAR sensor. As it will be shown, the lack of an adequate number of GB-SAR acquisitions will motivate the development of a new full-resolution PSI strategy, i.e., the TSSC approach presented in Chapter 7.

### 3.4 Non-Linear Estimation Block

The LEB provides just the main contribution of the displacement, i.e., the linear term, but it does not completely resume the complete differential phase. At the end of the LEB, an estimation of the absolute values of linear displacement rate  $\tilde{v}$  and topographic error  $\tilde{\varepsilon}$  have been obtained. The objective of this block of the CPT algorithm is to obtain the non-linear component of the displacement, also known as time-series. The rationale is to employ the estimates obtained at the end of LEB to clean fringes from the original interferograms and make easier the estimation of the non-linear component. The NLEB flow-chart is depicted in Fig. 3.14

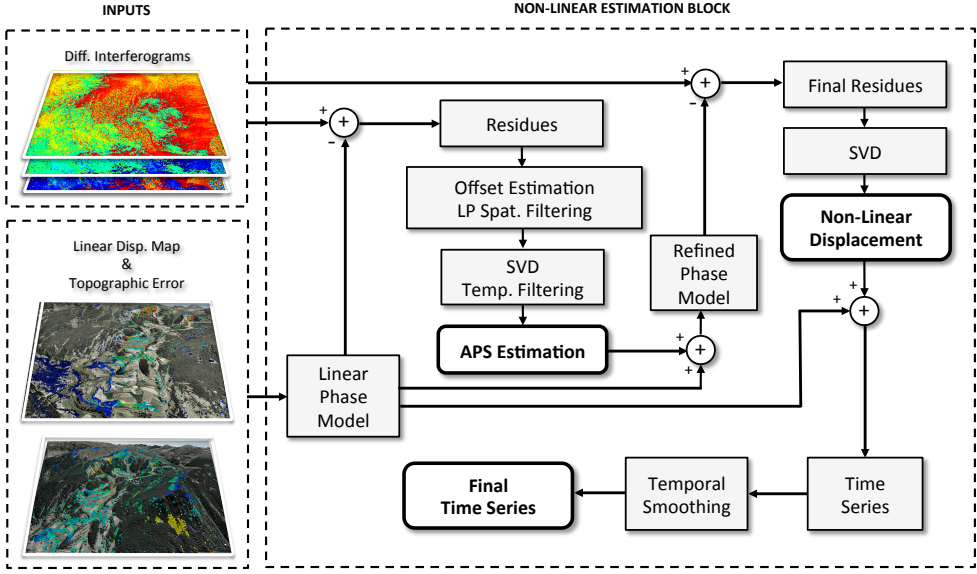


Figure 3.14: NLEB layout of CPT.

### 3.4.1 Residues calculation

Following the previous argument, the first step of the NLEB is based on calculating the so-called phase residues  $\varphi_i^{res}$ . With that purpose, the phase component  $\Delta\varphi_i^{\text{model}}$  corresponding to the linear model calculated in the previous step is subtracted from the original interferometric phases  $\varphi_i$  as follows

$$\varphi_i^{res}(T_i, B_n; x, y) = \varphi_i(T_i, B_n; x, y) - \varphi_i^{\text{model}}(T_i, B_n; x, y) \quad (3.28)$$

where the phase component corresponding to the linear model can easily be calculated from

$$\varphi_i^{\text{model}}(T_i, B_n; x, y) = \frac{4\pi}{\lambda} \cdot T_i \cdot \tilde{v}(x, y) + \frac{4\pi}{\lambda} \cdot \frac{B_{n,i}}{R_i \sin \theta_i} \cdot \tilde{\varepsilon}(x, y) \quad (3.29)$$

It is worth pointing out that this process is only applied over the survival PSCs after the integration process.

Once the linear component is retrieved from the original differential interferograms, the phase residues may be modeled as the sum of the following contributions

$$\varphi_i^{res}(T_i; x, y) = \varphi_i^{APS}(T_i; x, y) + \varphi_i^{non-lin}(T_i; x, y) + \varphi_i^{noise}(T_i; x, y) \quad (3.30)$$

Hereinafter, all the efforts will be addressed to separate the atmospheric artifacts  $\varphi_i^{APS}$  from the phase term causing the non-linear component  $\varphi_i^{non-lin}$ .

### 3.4.2 APS estimation

Once the residual phase is computed, the non-linear displacement term and APS estimation can be performed.

As seen in Section 2.4.2 of Chapter 2, APS is typically separated into one component related to tropospheric stratification and other to turbulent mixing. Regarding the tropospheric stratification several methodologies were reviewed in that Section. The first one was based on using multi-spectral data to exploit water vapor information provided by multi-spectral sensors, such as MERIS with ASAR data, but not possible with TerraSAR-X. The second approach consisted of the direct correction of tropospheric delays relying on external data collected by ground meteorological stations or accurate estimations of ZTD through GPS measurements. Unfortunately, no weather stations were available at *El Forn de Canillo*. Other strategies were based on exploiting weather forecasting models, but its poor spatial resolution prevents its application in complex phenomena such as the landslide of *El Forn de Canillo* characterized by local slides. Finally, empirical model-based techniques could be employed in order to exploit the existent correlation between APS and height. The main drawback of this approach is the possible underestimation of displacements when these are likely to be correlated with height. The use of these semi-empirical models is still an open issue and requires further investigation.

The methodology followed in this PhD Thesis is based on carrying out a filtering process, taking advantage of the particular temporal and spatial frequency behavior of APS [36], see Fig. 3.15. Atmospheric artifacts are characterized by having a low spatial frequency behavior for each interferogram due to its roughly 1 km correlation window [36]. As seen, in mountainous environments this is not true due to presence of rapid fringes of APS produced by tropospheric stratification. In order to compensate this effect, the correlation window over these environments should be reduced to 500 or even 250 meters. Regarding its temporal behavior, for a given pixel (belonging to an image, not to an interferogram), it can be considered as a white process, since atmospheric conditions change randomly for each acquisition date. Contrarily, non-linear displacement terms are considered to present a narrower spatial correlation window compared with APS and to behave low-pass along the temporal axis. The separation of the atmospheric artifacts and the non-linear component of displacement can hence be achieved carrying out a filtering process in both the spatial and the temporal domains [22]. The larger the number of images, the better the estimation of both components. It is worth pointing out that a complete separation in frequency is not possible due to the white process behavior of the atmospheric artifacts along the temporal axis, which fill the whole temporal spectra, as shown in Fig. 3.15.

According to the spectral properties described above, the next step of the NLEB is based on carrying out a spatial low-pass filtering of the residues. This step is implemented applying a two-dimensional moving averaging window of  $250m \times 250m$  (in order to face rapid tropospheric fringes). The objective is to reduce the non-linear displacement term keeping the atmospheric contribution. It must be pointed out that in order to apply the low-pass filtering only the survival PSCs are employed.

Once the low-pass filter is applied, the phase residues  $\varphi_i^{res,SLR}$  will contain the following contributions

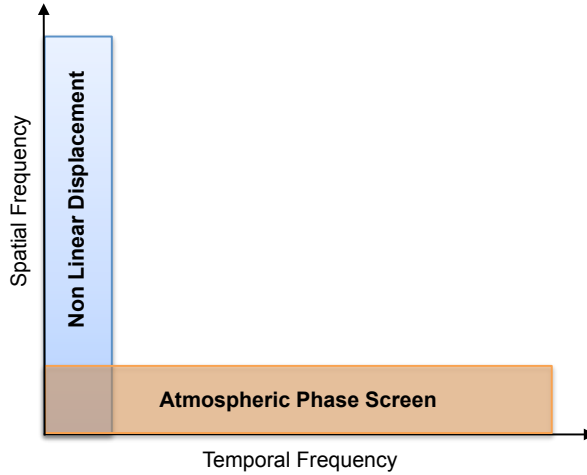


**Figure 3.15:** Frequency behavior of APS and non-linear displacement along the spatial and temporal axis.

$$\varphi_i^{res,SLR}(T_i; x, y) = \varphi_i^{APS}(T_i; x, y) + \varphi_i^{non-lin,SLR}(T_i; x, y) \quad (3.31)$$

where  $\varphi_i^{res,SLR}$  accounts for the Spatial Low Resolution (SLR) non-linear component of the displacement, while  $\varphi_i^{APS}$  is related to the total APS, since it is supposed to be not affected by the low-pass filtering.

If the AOI is affected by SLR non-linear displacements ( $\varphi_i^{non-lin,SLR} \neq 0$ ), this means there are non-linear displacements with an extension comparable or larger than the APS correlation window, the following step of the NLEB seeks for the separation between this SLR component and APS. This step consists of performing a high-pass filter along the temporal axis of  $\varphi_i^{res,SLR}$ .

At this point, it must be taken into account that  $\varphi_i^{res,SLR}$  do not follow the temporal order required to apply a temporal filtering. For this reason, these residues should be translated into their former absolute image phases. As it will be shown in the following, the Singular Value Decomposition (SVD) technique [183] can be applied in order to achieve this transformation. Prior to this, the low-pass version of the residues must be unwrapped and the different offsets among them must be accordingly compensated for. Notice that  $\varphi_i^{res,SLR}$  are smooth and, therefore, especially easy to unwrap, for instance, employing the software package SNAPHU. At the same time, the different offsets among them may be easily estimated through an histogram analysis.

At this stage, the vector to be estimated contains all the phase differences between consecutive acquisitions where each increment can be expressed as

$$\Delta\phi_k = \phi^{res,SLR}(t_{k+1}) - \phi^{res,SLR}(t_k) \quad 1 \leq k \leq N_{im} - 1 \quad (3.32)$$

where  $k$  accounts for the image acquisition time. Following this argument, the  $i$ -th

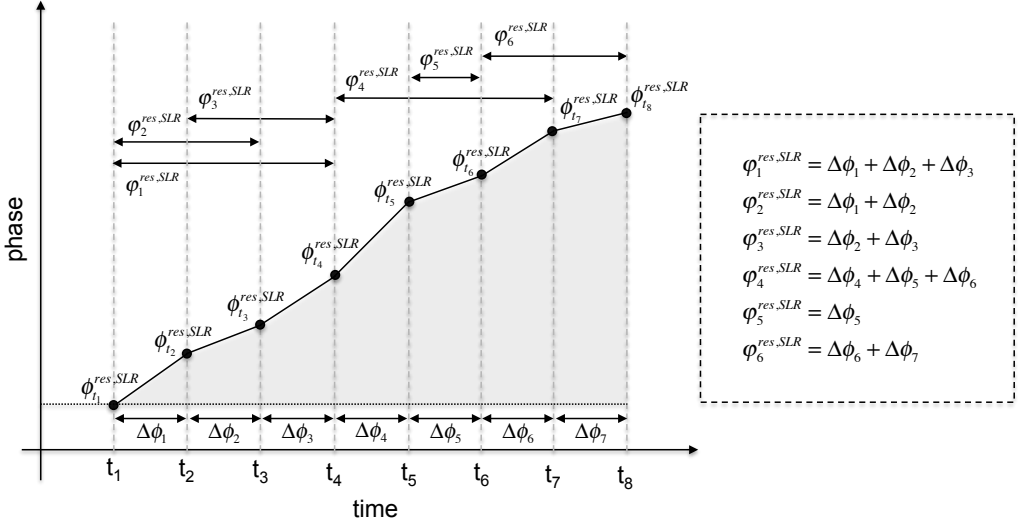


**Figure 3.16:** SVD construction problem example.

low-pass filtered interferometric phase residue may be expressed as follows

$$\varphi^{res,SLR}(T_i) = \sum_{k=t_{m,i}}^{t_{s,i}-1} \Delta\phi_k \quad (3.33)$$

where  $t_{m,i}$  and  $t_{s,i}$  refer to as the master and slave times belonging to the  $i$ -th interferogram, respectively. An example is depicted in Fig. 3.16.

The phase differences between consecutive acquisitions may be obtained solving the following linear equation system

$$\mathbf{B}\Delta\phi = \varphi^{res,SLR} \quad (3.34)$$

whose solution may be expressed as follows

$$\Delta\phi = B^\dagger \varphi^{res,SLR} = (B^T \cdot B)^{-1} \cdot B^T \cdot \varphi^{res,SLR} \quad (3.35)$$

and the SVD is employed to evaluate the pseudo-inverse matrix  $B^\dagger$  providing the least square solution of the linear system of equations. SVD gives the solution that best fits to data when the information is overlapped to ensure a certain continuity. If a gap of more than once cycle is present between constitutive acquisitions, the solution could not be correct. Further details about the mathematical formalism behind SVD are given in Appendix F.

After the inversion by means of SVD, the result is integrated. This result will contain an APS term, which now can be retrieved by means of high-pass temporal filtering, thus isolating the APS from the SLR non-linear displacement for each acquisition. Recall

that atmospheric artifacts are present at all frequencies while non-linear displacements are expected to have a low-pass temporal behavior. It is worth pointing out that the larger the number of images, the better the APS and the SLR non-linear displacement separation.

Notice that if the extension of the non-linear displacement is much smaller than the spatial window applied during the low-pass filtering, i.e., there is not any SLR non-linear displacement contribution, the low-pass filtered residues will only account for the APS and the offset of the residues. Following this argument, there is no need to perform all the steps described above (the SVD and the high-pass temporal filtering described above can be skipped). This is the case of *El Forn de Canillo* test site. The available ground truth in the AOI revealed that only the area of *Cal Borró-Cal Ponet* is affected by non-linear displacements. Since this area has a low extension (100 meters) compared with APS correlation window (250 meters), the estimation of APS can easily be addressed by means of low-pass filtering.

### 3.4.3 Time-series estimation

At this stage, the displacement information is not yet complete since details of the displacement at Spatial High Resolution (SHR) are missing. The procedure to retrieve the total non-linear contribution is described in the following.

Once the APS estimation has been obtained in the previous block, a new residual interferometric phase can be computed as follows

$$\begin{aligned}\varphi_i^{res,APS-free}(T_i; x, y) &= \varphi_i(T_i, B_{n,i}; x, y) - \varphi_i^{model}(T_i, B_{n,i}; x, y) - \varphi_i^{APS}(T_i; x, y) \\ &= \varphi_i^{non-lin}(T_i; x, y) + \varphi_i^{noise}\end{aligned}\tag{3.36}$$

where  $\varphi_i^{non-lin}$  now accounts for both, the SLR and the SHR non-linear displacement components.

Notice how now the new residues in (3.36) only accounts for the non-linear displacement component. By applying a new SVD process (as explained in the previous Section), the temporal profile of the non-linear displacement can easily be calculated. If a high non-linear displacement component is expected, prior to the SVD, residues should be unwrapped.

At this stage, the sum of the linear and non-linear contribution leads to the total displacement evolution or time-series of the displacement process. Optionally, time-series can be temporally filtered in order to reduce the remaining noise.

### 3.4.4 Time-series over El Forn de Canillo test site

To conclude this Section, a time-series example over the area of *Cal Borró-Cal Ponet* is presented in order to show the goodness of the techniques proposed, see Fig. 3.17.

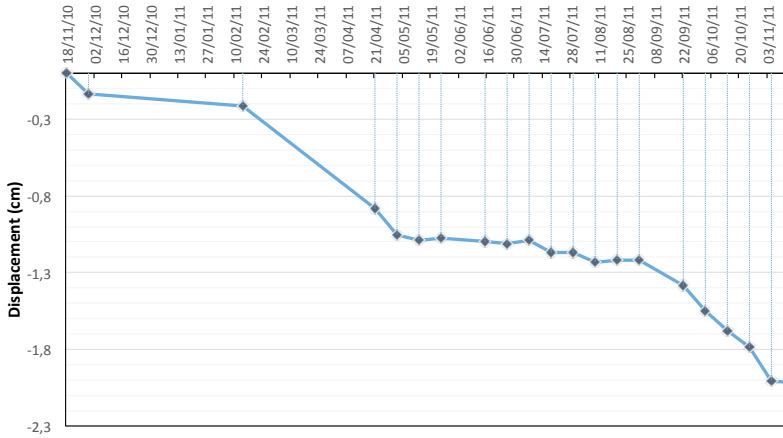


**Figure 3.17:** Time-series over the area of *Cal Borró-Cal Ponet* for the TerraSAR-X data set corresponding to *El Forn de Canillo*. Displacements are referred to the LOS.

Notice that the displacement is characterized by a non-linear component, presenting some acceleration and stabilization during the period of measures. As expected, it can be observed how the periods when the landslide experienced major accelerations are produced in the fall (during November 2010) and spring (from February to May 2011). This periods coincide with the major rainfall and snow melting events occurred. In the last period of the graph (September 2011), coinciding again with autumn's arrival, the landslide seems to accelerate again. This results show a high agreement with the conclusions extracted in [96].

Notice that displacements are again referred to the LOS. In the following Section, the way to convert both the linear displacement rate and the time-series values onto real ground displacements is described.

### 3.5 Final Product Layout Block

The last block of the CPT corresponds to the FPLB, which main objective is re-projecting the displacement values obtained in the LOS to the direction of the real ground displacement. In addition, a filtering of outliers based on SAR geometrical distortions and in the projection factor applied during the re-projection process, is presented.

SAR sensors are only sensitive to displacements produced along the LOS direction. Therefore, the measured displacements in the LOS are rarely the real ones, but a projection of them. This factor is extremely important in landslide monitoring applications, which typically occur over regions with steep topography. Over flat areas the interpretation of the LOS displacements does not represent any difficulty since the displacements are typically addressed as negative departing from the sensor, for subsidence phenomena, and positive approaching the radar, for uplift phenomena. On the contrary, when facing mountainous environments with steep topography the interpretation of final PSI products becomes more complex. In such regions, the real ground displacement of each spatial

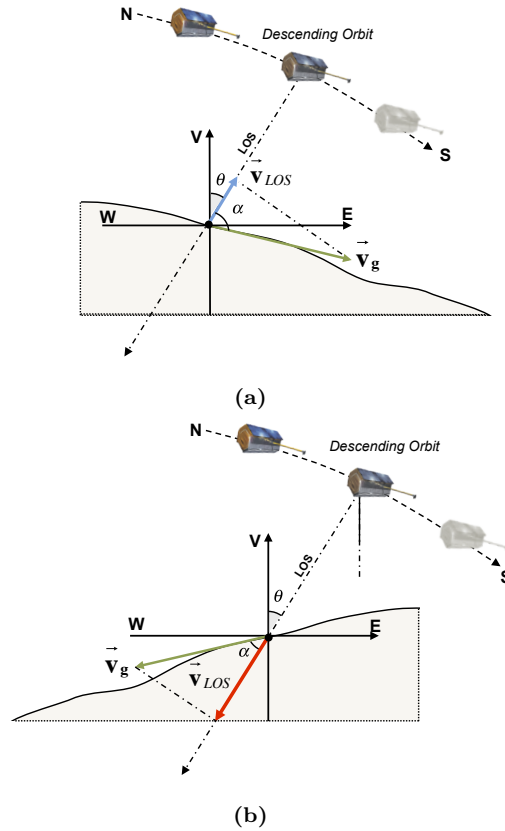


**Figure 3.18:** Geometry of acquisition under a down-slope displacement assumption for (a) a slope oriented facing the radar and (b) away from it. A descending orbit is considered for both cases.

point is related with the local slope and the more realistic assumption about the displacement direction, with no *a priori* knowledge, relies on considering that the displacement is produced along the steepest gradient of the terrain slope. If the slope of the mountain is facing the satellite, any displacement produced along the down-slope direction will be towards the satellite, see Fig. 3.18a. Contrarily, the same displacement will be detected as moving away from the SAR sensor if the slope is opposite, see Fig. 3.18b. This aspect should be also taken into account when planning the SAR acquisitions and was the main reason to select the descending mode for the TerraSAR-X data set corresponding to *El Forn de Canillo*.

Under the argument described above, the measured displacements in the LOS direction are a projection of the real ones and, hence, prior to any interpretation both the displacement rate maps and the time-series must be accordingly re-projected to follow the real ground displacement direction. This issue has been studied during this PhD Thesis, where a down-slope hypothesis has been developed for landslide monitoring applications.

Using a vector notation, the LOS and the ground displacement may be defined as

$$\begin{aligned}\mathbf{V}_{LOS} &= |\mathbf{V}_{LOS}| \cdot \hat{\mathbf{I}}_{LOS} \\ \mathbf{V}_G &= |\mathbf{V}_G| \cdot \hat{\mathbf{I}}_G\end{aligned}\quad (3.37)$$

where  $\mathbf{V}_G$  accounts for the ground displacement vector, this is the real displacement, and  $\mathbf{V}_{LOS}$  accounts for the LOS displacement vector, which represents the projection of the former along the LOS direction. The magnitudes  $|\mathbf{V}_{LOS}|$  and  $|\mathbf{V}_G|$  define the intensity of the displacement, and the unitary vectors  $\hat{\mathbf{I}}_{LOS}$  and  $\hat{\mathbf{I}}_G$  indicate the displacement direction. Since the former is only a projection of the latter, the magnitude of both displacement vectors can be related through a scalar product as follows

$$|\mathbf{V}_{LOS}| = |\mathbf{V}_G| \cdot \cos(\alpha) \quad (3.38)$$

where

$$\cos(\alpha) = \hat{\mathbf{I}}_{LOS} \cdot \hat{\mathbf{I}}_G, \quad (3.39)$$

being  $\alpha$  the angle between the unitary vectors.

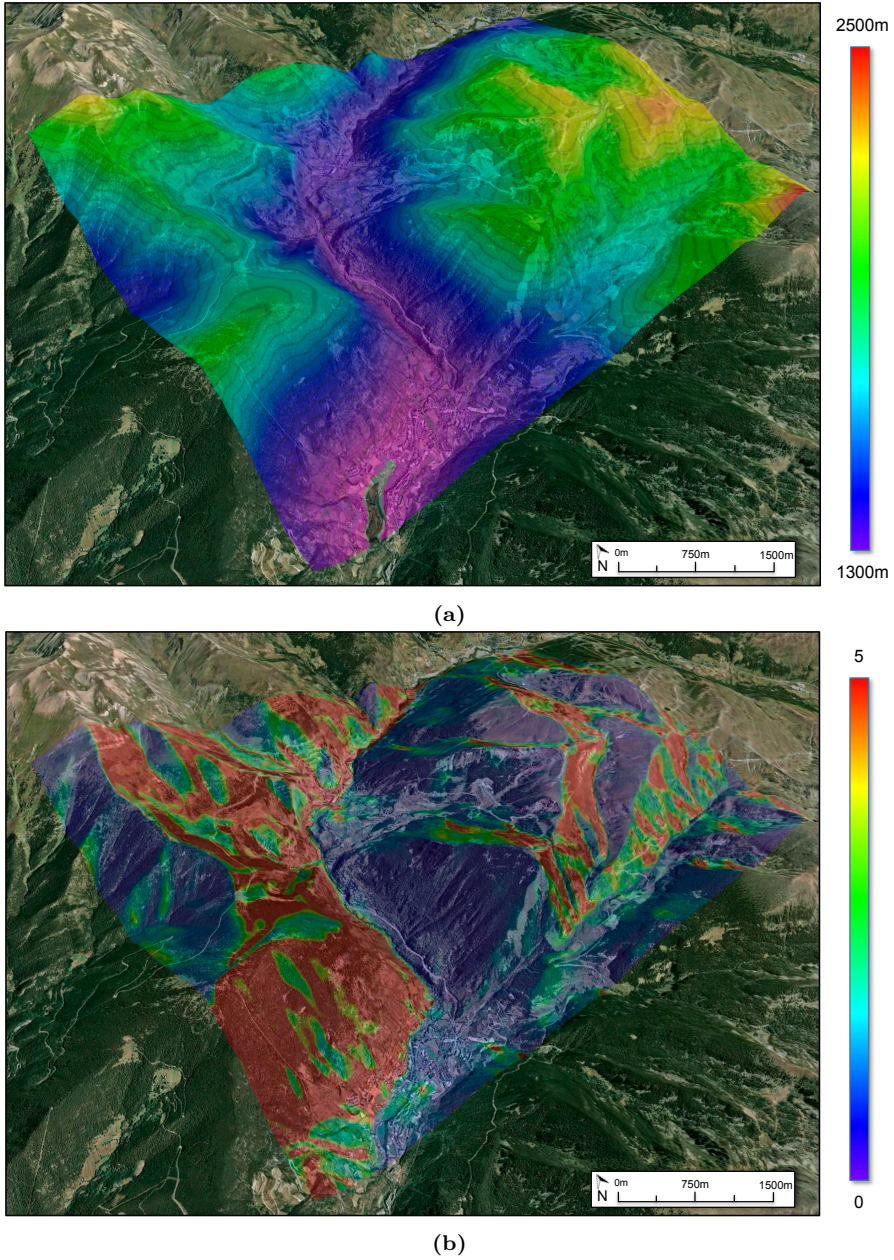
Under a nominal case of subsidence phenomena in urban scenarios,  $\alpha$  directly becomes the local incidence angle  $\theta$ . When facing landslide monitoring the problem becomes more complex since, as seen above, the real motion of a particular point is related with its local slope under a down-slope hypothesis. This information may be derived employing a DEM of the AOI. Then, the angle  $\alpha$  is directly obtained through (3.39). The quality of this process basically depends of the accuracy of the DEM employed.

Fig. 3.19 illustrates the down-slope projection factor calculated for the TerraSAR-X data set corresponding to *El Forn de Canillo*. Notice how, under the descending mode selected for this test site, the AOI presents low values of down-slope projection factor in general (around 1.5), this means with a good sensitivity in the LOS direction.

Once the PSI products are re-projected along the real ground displacement direction, some filtering can be applied to clean the final results. On the one hand, pixels exhibiting high values of down-slope projection factor, i.e., with a very bad sensitivity to the LOS direction, are filtered-out. In this context, those pixels presenting a projection factor value greater than 3 are relied as not-trusty and are typically removed from final PSI products. On the other hand, pixels affected by layover or high foreshortening may be also filtered-out. Fig. 3.20 shows the foreshortening and layover maps over the landslide of *El Forn de Canillo*. As illustrated, the AOI is free of SAR geometrical distortion effects.

At this stage, both the linear estimation and the final time-series can be geocoded in UTM coordinates, taking advantage of the topographic error height estimated during the LEB, and be visualized by using Geographic Information System (GIS) software or a virtual globe viewer.

The final geocoded down-slope results over *El Forn de Canillo* for both the orbital and the ground-based data sets available, and its comparison with the ground truth available, will be presented in the final Chapter 8, for both the classical approaches (reviewed in this Chapter) and the new PSI approach developed in this PhD Thesis (the TSSC approach, presented in Chapter 7).



**Figure 3.19:** (a) SRTM DEM of 90 m resolution corresponding to the landslide of *El Forno de Canillo*. (b) Down-slope projection factor for the TerraSAR-X data set.

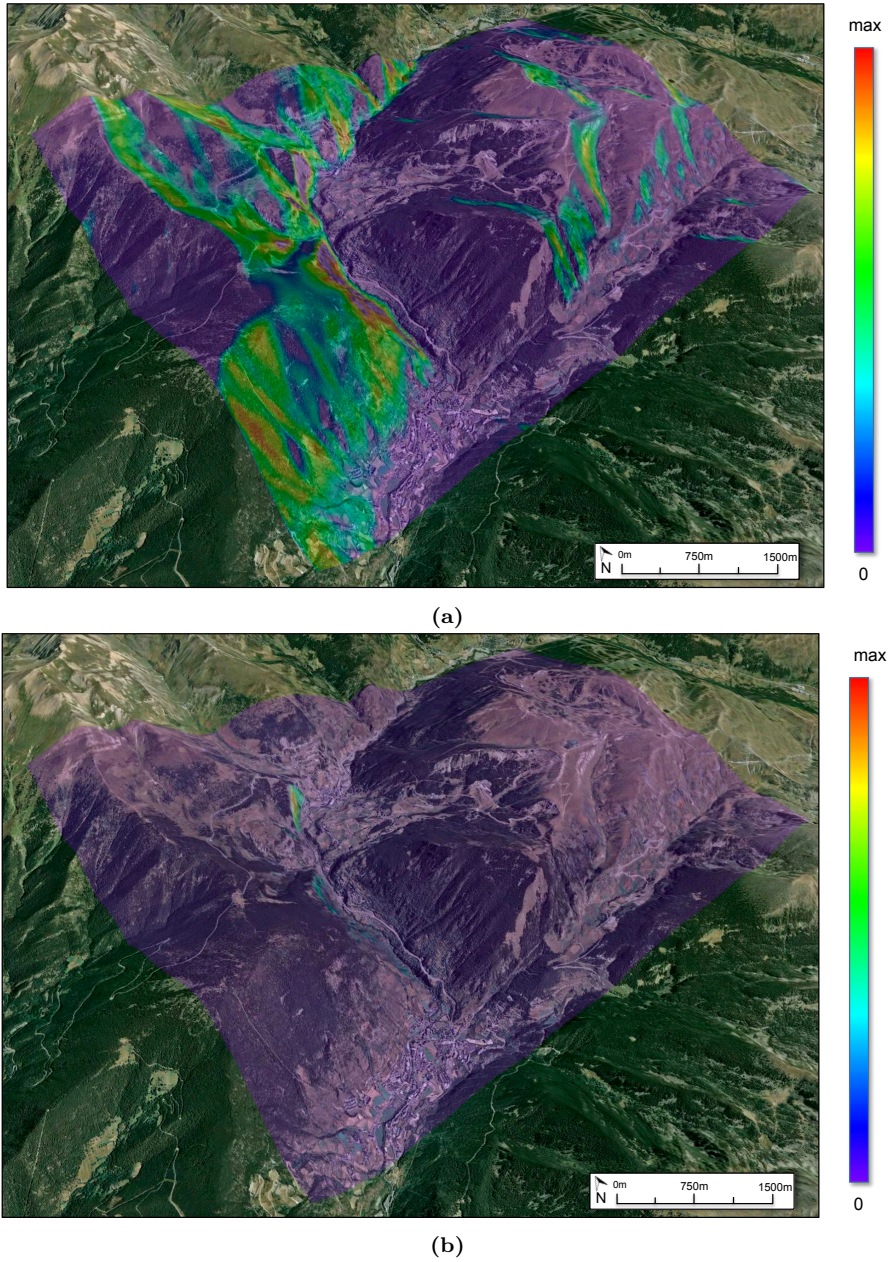


**Figure 3.20:** (a) Foreshortening and (b) layover maps for the TerraSAR-X data set corresponding to the landslide of *El Forn de Canillo*.

### 3.6 Concluding remarks

The exploitation of the interferometric phase is compromised by the impact of geometrical and temporal decorrelation phenomena. The presence of APS also difficults the applicability of classical DInSAR techniques. In order to overcome these limitations, PSI techniques are typically addressed.

In this Chapter, a description of PSI techniques, basing on the CPT algorithm developed by the RSLab of the UPC, has been presented. This technique allows the estimation of the linear and non-linear components of the displacement, the topographic error, as well as the atmospheric artifacts from a multi-temporal set of differential interferograms.

The objective of the first block of the CPT is to obtain a selection of differential interferograms and detect the so-called persistent scatterers. On the one hand, an improved selection of differential interferograms has been presented with the objective to reduce the impact of interferometric pairs largely affected by temporal and geometrical decorrelation phenomena. On the other hand, classical pixel selection criteria have been reviewed, highlighting the benefits of employing full-resolution techniques to improve the density of points in this type of scenarios. Finally, the employment of the SVA technique has been proposed to prevent the inclusion of side-lobes during the PSI processing.

During the LEB of the CPT, the phase linear parameters are extracted. Consequently, the linear velocity and the topographic error map of the selected pixels are obtained. The use of redundant networks has been proposed at this stage to face the low density of persistent scatterers present in this type of scenarios. Results over *El Forn de Canillo* employing the TerraSAR-X data set have been presented in order to demonstrate the benefits of full-resolution PSI, such as the PS approach, for landslide monitoring applications. The increase in pixels' density (five times more compared with the coherence stability approach), especially, over areas characterized by exposed rocks surrounded by vegetation, have improved the delineation and characterization of the landslide.

Employing the results obtained in the LEB block, a third block called NLEB, which is devoted to the extraction of the non-linear phase components, is carried out. In this block, the non-linear displacement component and the atmospheric artifacts are estimated for each of the participant images, after cleaning the original phases from the linear parameters obtained in the previous block. The way to face rapid tropospheric artifacts correlated with the topography has been put forward. Finally, time-series over *El Forn de Canillo* have been presented showing a high agreement with the periods of rainfalls and snow melting during the monitoring interval.

Finally, the FPLB block of the CPT is addressed to re-project the LOS velocity onto the real ground displacement direction and filter-out possible outliers in the results. This step is extremely important in landslide environments where a down-slope hypothesis must be applied to allow the correct interpretation of results.

As summary, we can say that the improved resolution capabilities of the sliding-spotlight TerraSAR-X imaging mode allows the use of full-resolution PSI techniques, even in natural environments largely vegetated. The presence of few man-made structures, outcrops or exposed rocks allows unprecedented quantities of measurements, not possible before the arrival of this new generation of SAR sensors. The results showed demonstrate that when the number of SAR images is adequate (more than 20) a reliable full-resolution

PSI can be performed through the  $D_A$  estimator, even in challenging scenarios such as *El Forn de Canillo*.

The following Chapters are addressed to compare the space-borne results showed in this Chapter with the ones obtained with the RikSAR sensor. As it will be shown, the lack of an adequate number of GB-SAR acquisitions will motivate the development of a new full-resolution PSI strategy, i.e, the TSSC approach, which is presented in Chapter 7. Prior to this GB-InSAR and GB-SAR PSI techniques will be formulated putting special attention in the way to compensate APS and exploit the polarimetric capabilities of the RiskSAR sensor.



# 4

## CHAPTER 4

# GB-IN SAR AND APS COMPENSATION

---

IN the previous Chapters the basic concepts of InSAR, DInSAR and PSI have been introduced focusing in space-borne SAR sensors. From this point, the adaptation of such techniques to work with zero-baseline GB-SAR data, particularly with the RiskSAR sensor developed by the RSLab of the UPC (described in Section 1.4.2 of Chapter 1) are presented. In this Chapter, a complete description of GB-InSAR and a first approximation to GB-SAR PSI are proposed focusing in landslide monitoring applications.

GB-InSAR is a remote sensing technique ideal for the monitoring of small-scale areas, which ensure a high stability of the platform, an adaptable revisiting time in function of displacement phenomena characteristics, and the possibility to fit the illumination angle for a specific site geometry. This features make GB-InSAR techniques a suitable alternative, sometimes complementary, to space-borne solutions.

As reviewed in Section 2.4 of Chapter 2, when space-borne SAR solutions are adopted for the monitoring of an affected area there are a large number of decorrelation sources that

affect the coherence and thus compromise the quality of the interferometric phase. These are the thermal noise, temporal decorrelation (due to the temporal changes in the AOI), geometric decorrelation (due to the non-zero baseline configuration of space-borne sensors), volumetric decorrelation (caused by the vertical distribution of scatterers), Doppler Centroid differences (when an interferometric pair is acquired with different Dopplers), but also factors inherent to the processing like inaccuracies on the co-registration. Other sources of noise that impact the PSI processing are associated to orbital errors, the lack of precision in the DEM used to remove the topographic component during the generation of differential interferograms and, finally, atmospheric artifacts. In GB-InSAR, the instrument is firmly anchored on the same position for all acquisitions in a zero-baseline configuration and, for this reason, most of the previously sources of noise do not affect data. In fact, APS represents the most relevant artifact of distortion between interferometric GB-SAR pairs. Prior to the application of any PSI technique, APS must be correctly estimated and consistently compensated for in order to obtain reliable displacement maps estimations. For this reason, the efforts of this Chapter are addressed to the understanding and mitigation of the negative impact of APS in GB-SAR measurements.

Several studies for APS compensation with GB-SAR data are available in the literature. References [70] and [184, 185], present compensation techniques basing on semi-empirical models of APS over the PS or the high-coherence scatterers within the area under study, respectively, without the use of any external information. In reference [67], authors propose a solution based on extrapolating APS information from known motionless GCPs, that means, exploiting *a priori* information of the AOI. Finally, in reference [186] the compensation is addressed basing on in-situ meteorological information. From all these available methods, model-based solutions have proven to be very effective without the employment of meteorological data or stable GCPs. Unfortunately, the linear approximation proposed in [184, 185] is not sufficient in mountainous regions. As it will be shown along this Chapter, in such regions, atmospheric artifacts are intense, deeply correlated with the topography and highly dynamic in time.

In this framework, an extension of the model-based method described in [184, 185], now taking into account the relation of APS with topography, is proposed. Furthermore, the adaptation of such technique to work with PolSAR data is presented, showing a noticeable improvement in the compensation process. The method proposed is validated in the mountainous environment of *El Forn de Canillo* using the GB-SAR fully-polarimetric data set presented in Section 1.4.3 of Chapter 2. First, the impact of the severe atmospheric fluctuations among GB-SAR measurements is carefully analyzed. Hence, the methodology to estimate and compensate APS from a set of interferograms is put forward. A complete description of GB-InSAR and a first approximation to zero-baseline PSI is finally presented in order to validate the results obtained making a cross-correlation with the displacement results obtained with the TerraSAR-X data set available.

The content of this Chapter corresponds to the following publication:

R. Iglesias, X. Fabregas, A. Aguasca, J. J. Mallorqui, C. López-Martínez, J. A. Gili, and J. Corominas, “Atmospheric Phase Screen Compensation in Ground-Based SAR With a Multiple-Regression Model Over Mountainous Regions,” *IEEE Transactions on Geoscience and Remote Sensing*, vol. 52, no. 5, pp. 2436-2449, May 2014.

**ATTENTION :**

Pages 123 to 136 of the thesis containing this article:

**Atmospheric Phase Screen Compensation in Ground-Based SAR With a Multiple-Regression Model Over Mountainous Regions**

Rubén Iglesias, *Student Member, IEEE*, Xavier Fabregas, *Member, IEEE*, Albert Agasca, *Member, IEEE*, Jordi J. Mallorqui, *Senior Member, IEEE*, Carlos López-Martínez, *Senior Member, IEEE*, Josep A. Gili, and Jordi Corominas

are available at the editor's web

**<http://ieeexplore.ieee.org/xpl/articleDetails.jsp?arnumber=6553066>**

# 5

## CHAPTER 5

# POLARIMETRIC PHASE QUALITY OPTIMIZATION

---

IN the previous Chapter GB-InSAR techniques have been presented. Concretely, the way to face APS over mountainous environments, main source of errors when a GB-SAR solution is adopted for the monitoring of a certain AOI, has been put forward. In this Chapter a way of improving GB-InSAR techniques in terms of density and quality is discussed.

As seen along this PhD Thesis, PSI techniques present clear advantages in terms of density, coverage and accessibility compared with traditional geotechnical devices. Despite this, they also exhibit some limitations, especially over natural environments such as *El Forn de Canillo*. Mainly due to decorrelation phenomena, displacement information cannot be exploited from all pixels within the illuminated scenario since only a limited number of them fulfill the phase quality requirements to be exploited during PSI. In landslide monitoring applications, improving the number of PSCs results of crucial importance. This fact allows the achievement of more robust networks of persistent scat-

terers, thus favoring the reliable estimation of displacement maps in a major number of areas, as seen in Chapter 3.

Mainly due to the lack of long-term PolSAR data, the development of differential interferometric techniques has been traditionally limited to the single-polarimetric case. However, during the last years, several orbital SAR sensors, such as ALOS PALSAR, RADARSAT-2 or TerraSAR-X, have been improved with polarimetric capabilities, thus allowing the extension of traditional PSI techniques to the polarimetric case. This concept was first introduced in [49, 50, 79] for its application to zero-baseline GB-SAR data. For the first time, the concept of PolDInSAR, which has demonstrated to outperform classical DInSAR, was introduced. In fact, its application to space-borne data [187–190] has been presented recently. The objective of this Chapter is to extend this research, making use of the mathematical formulation presented in Section 2.5 of Chapter 2, in order to demonstrate its performance in landslide monitoring applications.

The rationale of PolDInSAR techniques is improving the number of reliable pixel candidates during the pixel selection step, taking advantage of the polarimetric capabilities of data. In classical InSAR or DInSAR formulation, only a single-polarimetric channel is considered. This means that all pixels involved in the processing belong to the same polarimetric channel. The rationale of polarimetric optimization techniques is to enhance the phase quality of the interferograms available by combining adequately different polarimetric channels in order to exploit a major number of PSCs in the later PSI processing.

In this framework, different approaches will be evaluated. In the Best approach, for each pixel of the image the polarimetric channel providing the best response in terms of phase quality, is selected. Despite the significant improvement in terms of pixels' density achieved with this method, this strategy does not completely exploit the potentials of polarimetry. The objective of the other two approaches is to find the optimum scattering coefficient (Equal Scattering Mechanism (ESM)) or the best polarimetric basis transformation (Sub-Optimum Scattering Mechanism (SOM)), applied along the whole PolSAR data set that maximizes the phase quality. All the algorithms, originally defined for the coherence stability method, have been extended to work with the  $D_A$  approach in this PhD Thesis.

The techniques presented are validated in the mountainous environment of *El Forn de Canillo* using the GB-SAR fully-polarimetric data set presented in Section 1.4.3 of Chapter 2. Since the number of images available is short for this data set, thus compromising the application of the  $D_A$  approach (as seen in Section 3.2.3 of Chapter 3), a study corresponding to an orbital PolSAR data set based on 34 Fine Quad-Pol RADARSAT-2 acquisitions, from January 2010 to May 2012, over the metropolitan area of Barcelona, is also presented. The main differences and key processing particularities between working with zero-baseline GB-SAR and space-borne SAR data are largely discussed.

The content of this Chapter corresponds to the following publication:

R. Iglesias, D. Monells, X. Fabregas, J. J. Mallorqui, A. Aguasca, and C. López-Martínez, "Phase Quality Optimization in Polarimetric Differential SAR Interferometry," *IEEE Transactions on Geoscience and Remote Sensing*, vol. 52, no. 5, pp. 2875-2888, May 2014.

The recent launch of the satellites ALOS-2 and Sentinel-1, with polarimetric capabilities, highlight the significance of this topic.

**ATTENTION !**

Pages 139 to 152 of the thesis containing this article:

**Phase Quality Optimization in Polarimetric Differential SAR Interferometry** Rubén Iglesias, *Student Member, IEEE*, Dani Monells, *Student Member, IEEE*, Xavier Fabregas, *Member, IEEE*, Jordi J. Mallorquí, *Senior Member, IEEE*, Albert Aguasca, *Member, IEEE*, and Carlos López-Martínez, *Senior Member, IEEE*

are available at the editor's web

<http://ieeexplore.ieee.org/xpl/articleDetails.jsp?arnumber=6553165>